

**Optical Properties of Non-Spherical Particles of Size Comparable to the
Wavelength of Light: Application to Comet Dust.**

Padmavati A. Yanamandra-Fisher and Martha S. Hanner

Jet Propulsion Laboratory, California Institute of Technology

Pasadena, CA 91109

Submitted to *Icarus*, August 1997

28 Pages

37 Figures

4 Tables

Send correspondence to:

Dr. Padmavati A. Yanamandra-Fisher

Mail Stop 169-237

Jet Propulsion Laboratory

4800 Oak Grove Drive

Pasadena, CA 91109

e-mail: padma@durga.jpl.nasa.gov

v-mail: (818) 354 - 2321

fax: (818) 393-4619

Running Title: OPTICAL PROPERTIES OF NON-SPHERICAL PARTICLES: COMET DUST

Running Authours: YANAMANDRA-FISHER ANI HANNER

ABSTRACT

Scattering calculations of non-spherical particles have been carried out in order to explain observed optical properties of cometary dust. We focused on two optical properties of cometary dust sensitive to particle shape: negative linear polarization at phase angles $\leq 21^\circ$ and the $11.2 \mu\text{m}$ silicate emission feature. The discrete dipole approximation (DDA) method was employed to compute the scattering matrix for non-spherical silicate and absorbing particles of size comparable to the wavelength.

Silicate particles with a variety of shapes and size parameter $X_{eq} \sim 2.5$, corresponding to a linear dimension of $0.5 - 1.0 \mu\text{m}$, can produce negative linear polarization at small phase angles, whereas carbon particles produce a strong positive maximum of polarization near phase angles of 90° . Mixtures of silicate and carbonaceous material, on a scale small compared to the wavelength, eliminate the negative polarization in this size range; however, macroscopic mixtures of silicate and carbon could yield the observed negative linear polarization at low phase angles ($\leq 21^\circ$) and a maximum positive polarization at phase angle of 90° .

The position of the $11.2 \mu\text{m}$ thermal emission peak observed in comets, attributed to crystalline olivine, depends strongly on particle shape even for particles much smaller than the wavelength and can be matched with anisotropic Mg-rich olivine for our model tetrahedral or moderately elongated bricks. Spheres and extreme shapes, such as disks or needles, appear to be ruled out. Approximately 20% crystalline olivine and 80% disordered olivine reproduces the observed spectra of comets with comparable peaks at 10 and $11.2 \mu\text{m}$, e.g., P/Halley, Bradfield 1987 XXIX, Mueller 1993a, C/1990 K1 (Levy 1990 XX) and C/1995 O1 (Hale Bopp).

Our study provides important results and essential guidelines for characterization of non-spherical monomers or constituent particles selected for aggregate models of cometary dust since

it, is well known that the scattering properties of aggregates depend on the scattering properties of their constituent particles.

I. INTRODUCTION

Interpretation of remote sensing observations of cometary dust requires understanding the light interaction with small particles, which depends on their shape, size, and composition. The present study was motivated by two cometary observations that depend strongly on particle shape: (i) negative linear polarization at small phase angles ($\leq 21^\circ$) at visual wavelengths (Dollfus *et al.* 1988, Levasseur-Regourd *et al.* 1996) and (ii) thermal emission peak at $11.2 \mu\text{m}$, attributed to the presence of crystalline olivine grains (Hanner *et al.* 1994a,b and references therein). These observations are shown in Figure 1.

Captured interplanetary dust particles (IDPs) thought to be of cometary origin frequently have aggregate structure comprised of solid grains with linear dimension a few tenths of a micron, corresponding to a size parameter $X_{eq} = 2-5$ at visual wavelengths (Brownlee 1985). The $3-20 \mu\text{m}$ thermal energy distribution and the presence of a silicate emission feature indicate that the optically dominant particles in many comets are about $1 \mu\text{m}$ or less in size (Hanner 1983; Hanner *et al.* 1985). The relevant range of particle sizes to be investigated in this study is thus $0.1 - 1 \mu\text{m}$.

Classically, the problem of light scattering can be solved exactly using Mie theory for spheres (van de Hulst 1957). However, spheres introduce resonances in the scattered intensity and polarization which are not present for non-spherical particles and not observed in comets. Modern high-speed computers and available numerical codes mean that we are no longer restricted to spheres, but are free to model the light interaction with particles of arbitrary shape. Considerable work has been done modeling the scattering properties of aggregate particles. However, almost all of the aggregates modeled have been composed of spherical particles whose size is smaller than the wavelength, essentially in the Rayleigh regime. Such aggregates cannot reproduce the observed negative linear polarization at low phase angles at visual wavelengths (Kozasa *et al.*, 1992, 1993;

Perrin and Sivan, 1991). West (1991) and Zerull *et al.* (1993) have demonstrated both by computations and laboratory measurements that scattering properties of an aggregate particle are strongly influenced by the scattering properties of its individual constituent particles. This important result means that the optical properties of non-spherical particles comparable in size to the wavelength of light have to be understood before modeling cometary dust as aggregate particles.

Thus, the purpose of this paper is to characterize the influence of particle shape, size, porosity, and composition on the scattering properties (polarization and phase function), for moderate size parameters, $X_{eq} = 2 - 5$, comparable to the optically dominant particle size range in cometary dust. We also investigate the effect of particle Shape on the $11.2 \mu\text{m}$ spectral feature of crystalline olivine particles with the same linear dimensions as those studied at visual wavelengths. We seek to answer two questions: Can non-spherical particles of size comparable to the wavelength give rise to negative polarization at small phase angles ($< 210^\circ$)? Can these particles simultaneously produce the $11.2 \mu\text{m}$ silicate feature similar to that observed in comets?

This study is a necessary and essential first step toward realistic modeling of comet dust as aggregates composed of non-spherical monomers having dimensions comparable to the wavelength of incident radiation.

II. METHOD

Numerical Method

We chose to employ the discrete dipole approximation (DDA) technique (Purcell and Pennypacker, 1973; Draine, 1988; Goodman *et al.*, 1990). The DDA method allows an arbitrarily shaped particle to be represented by an ensemble of N electromagnetically interacting dipoles on a lattice grid. Each dipole radiates a dipole field in response to the incident radiation and the radiated fields of all other dipoles in the ensemble. We have used the DDSCAT (version 4a) code, originally devel-

oped by Draine (1988) and modified by Goodman *et al.* (1990) to employ a fast Fourier transform (FFT) algorithm to perform the calculations efficiently.

The constraints for the validity of the DDSCAT code are: (i) the lattice spacing d to be small enough compared with the wavelength of light in the target medium, $kd|m| \leq 0.5$, where k is the wave number and m is the complex index of refraction; (ii) d must be small enough to describe the target particle shape satisfactorily; and (iii) $|m| \leq 2$; otherwise error in polarization is too large in the surface monolayer of the particle (Draine and Flatau, 1994). The constraints on d determine the number of dipoles required. We define the equivalent volume size parameter, $X_{eq} = ka_{eq}$, where a_{eq} is the radius of a sphere of equivalent volume to the target particle. The number of dipoles is then equal to $N = \left(\frac{4\pi}{3}\right)\left(\frac{a_{eq}}{d}\right)^3$. At our reference wavelength of $0.6 \mu\text{m}$ and size parameter X_{eq} from 2 to 5, the number of dipoles required for the polarization calculations ranges from 3000 to 40,000. Tests were run with DISCAT for spherical particles and compared with Mie theory calculations to confirm that the number of dipoles was adequate. Memory size needed for storing the dipole array imposes a practical limit to the size parameter that can be studied.

The target particle is fixed relative to a coordinate system oriented on a rectangular grid with respect to the direction of the incident radiation by the specification of three rotation angles: θ , β and ϕ . The angles θ and ϕ position the target particle with respect to the direction of the incident radiation while the third angle, β , defines the rotation of the target particle in its frame of reference. When the three angles are equal to zero, the target frame is parallel to the lattice frame. Random orientation of the target is achieved by sampling the three angles (θ, β, ϕ) over the intervals (0,180), (0,360), (0,360) respectively. While the computed absorption efficiency factor, Q_{abs} , is not very sensitive to the number of orientations averaged, polarization is extremely sensitive. We average over at least 90 orientations in the $(0, \beta)$ space and at least 70 samples in the third angle, ϕ , for a total of 6300 orientations for small size parameters (≤ 3) and 56 orientations in (θ, β) for

Table 11A lists all 67 cases that were studied. All input parameters defining each case are listed, followed by the calculated optical properties such as the various efficiency factors; single scattering albedo, ω_o ; the asymmetry factor, g ; forward diffraction peak ($P^{11}(00)$), back scattering ($P^{11}(1800)$) and the enhancement in the backscatter direction, defined as the ratio $P^{11}(180^\circ)/P^{11}(1500)$. The following trends are evident from Table 11A for homogeneous particles: (i) the maximum scattering efficiency factor (Q_{sca}) for silicate particles occurs at larger volume equivalent size parameter for the elongated particles; (ii) the absorption efficiency factor (Q_{abs}) for carbon particles displays a maximum for a size parameter about 2, for spheres, brick (5:2:1), and tetrahedra; (iii) single scattering albedo increases with size for carbon particles, approaching a value of 0.5 at $X_{eq} \sim 5$, independent of shape; (iv) asymmetry parameter increases with size, as expected and (v) enhancement in the backscatter direction is evident in silicate particles of all shapes and is reduced in the carbon particles. Inhomogeneity of the particle introduced as porosity or heterogeneity changes some of these trends, as indicated in Table II B. Porosity makes the particles more forward diffracting. A 50:50 mixture of silicate: carbon decreases the single scattering albedo of the particle to a value of 0.5 and suppresses the backscatter enhancement as the heterogeneous particle becomes dominantly absorbing.

We interpret the visual polarization, phase function and silicate thermal emission observed in comets in context of our particle models in detail in the following sections. In sections A and B, we investigate the influence of particle shape, size and composition on linear polarization ($(-1001^{2L})/1^{11}$) and phase function (P^{11}), where P^{11} and P^{21} are elements of the phase matrix, computed by the DDSCAT algorithm. The silicate emission feature is discussed in section C.

A. Polarization

The main characteristics of cometary polarization curve are: (i) negative polarization ($\sim -2\%$)

at low phase angles ($\leq 210^\circ$); (ii) an inversion angle or neutral point, θ_0 , about 22° ; (iii) a slope, h , of $\sim 0.2\%$ per deg at the point of inversion and (iv) maximum polarization (P_{max}) near phase angle of 95° ; with recent evidence for the existence of a dichotomy between comets of different maximum polarization (Dollfus *et al.*, 1988; Levasseur-Regourd *et al.*, 1996). A composite plot of the polarization versus phase angle for many comets, adapted from Levasseur-Regourd *et al.* (1996) is shown in Figure 1a.

Homogeneous Compact Particles

The DDSCAT algorithm allows the selection of several regular particle shapes. Of these, we selected the following shapes: sphere for a benchmark between DDSCAT and Mie calculations and also because it is the basic shape studied by almost all investigators; brick represents either an elongated or a flat plate-like particle with an appropriate selection of aspect ratio; cylinder and hexagonal prism are other examples of elongated particles; cube is an equidimensional compact particle, whereas the tetrahedron represents an equidimensional particle with greater surface area than the other shapes for a given size.

Figures (2) - (4) show the development of the polarization curves for spheres, bricks and tetrahedra as the equivalent volume size parameter (X_{eq}) increases from 1 to 5. The polarization is essentially that of a Rayleigh scatterer for $X_{eq} \leq 1$.

Sphere. Spheres were studied with the DDSCAT program as our reference shape. The results were checked against Mie calculations to ensure the proper performance of the algorithm. We impose the condition that the absolute error in polarization be less than 10%, where absolute error is defined as $((\text{pol}_{Mie} - \text{pol}_{DDA}) / (\text{pol}_{Mie})) * 100$. The curves for spheres exhibit various maxima and minima expected from the constructive and destructive interference of light waves with the particle (Figure 2). Silicate spheres exhibit large negative polarization for $X_{eq} \geq 1.75$, but small maximum positive

polarization (Figure 2a). Although carbon spheres exhibit mainly positive polarization, in contrast to silicate *spheres*, there are some size parameters ($X_{eq} = 1.5, 5$) for which negative polarization appears at small phase angles (Figure 2b).

Brick. Two types of bricks were studied: an ‘‘elongated’’ brick (a) with ratio of principal axes defined as (5:2:1) and a ‘‘flat’’ brick (b) with the ratio of principal axes defined as (5:5:1). Both silicate and carbon bricks show large positive polarization with a broad maximum that shifts in position with size (Figure 3). Only for $X_{eq} = 5$ silicate brick does a small negative polarization appear at small phase angles. In the case of the elongated brick (a), no negative polarization is evident for both silicate and carbon particles of $X_{eq} = 2.5$, but $X_{eq} = 5$ silicate particles display a negative branch of linear polarization, similar to brick (b) (Figures 6, 7).

Tetrahedron. The strong oscillations observed in the polarization by spheres are much reduced in the polarization curves for tetrahedra (Figure 4). Silicate tetrahedral, with $X_{eq} \geq 2.5$, develop a small negative branch of linear polarization at small phase angles, qualitatively similar to the observed cometary dust polarization. Figure (5) shows the onset of negative polarization in the silicate tetrahedron. As we increase the size parameter from 2 to 2.5, we observe that scattering from a silicate tetrahedral particle develops a negative branch at intermediate phase angle of 60° , which gradually shifts to phase angle of 300° . A tetrahedral particle of size parameter 2.5 corresponds to a physical dimension of about one micron edge length, which is comparable to a typical dimension of grains in captured IDPs. The carbon tetrahedron does not develop negative polarization nor does the maximum positive polarization decrease very much with size.

Figures 6 and 7 compare the polarization for various shapes at $X_{eq} = 2.5$ and $X_{eq} = 5$. For $X_{eq} = 2.5$ silicate particles, several shapes have small negative polarization at low phase angles, whereas spheres display large negative linear polarization (Figure 6a). In contrast, this negative branch of linear polarization is generally absent for $X_{eq} = 2.5$ carbon particles (Figure 6b). The

four elongated particles (brick (a), brick (b), cylinder and hexagonal prism) have similar curves. The cube exhibits resonances reminiscent of a sphere; it would not be a good choice of monomer shape for modeling irregular particles. At $X_{eq}=5$, silicate particles of all shapes have oscillations of varying amplitudes including negative polarization at small phase angles (Figure 7a). Silicate bricks most closely resemble the cometary dust polarization. All carbon particles with $X_{eq}=5$ exhibit strong positive polarization] $\sim 50\%$ (Figure 7b). This is similar to the polarization measured for large irregular absorbing particles ($X_{eq} \approx 20 - 30$) by Giese *et al.* (1978).

In summary, non-spherical, compact or elongated silicate particles of linear dimension comparable to the wavelength tend to have negative polarization at small phase angles ($\leq 21^\circ$) and moderate positive polarization at intermediate angles ($60 - 120^\circ$), qualitatively similar to cometary dust polarization and very different from scattering by spheres of similar size.

Inhomogeneous Particles

Porous

In order to study the effect of porosity on the polarization, we created porous particles by random removal of single dipoles from the homogeneous dipole array. We define porosity as the ratio of (number of dipoles removed)/(total number of dipoles); the lattice array of dipoles is not changed, but the envelope of the dipoles now includes voids.

Figures 8 and 9 illustrate polarization curves for porous silicate and carbon spheres and tetrahedra with $X_{eq}=2.5$. The introduction of porosity produces significant changes, particularly for phase angles less than 90° . For the silicate particles, negative polarization is greatly reduced (spheres) or eliminated (tetrahedra). In carbon spheres, porosity actually introduces negative polarization at $0 < 60^\circ$. In the case of tetrahedra, removal of dipoles yields a shape different from that of the original particle, creating a smaller, more compact particle. Hence, the polarization changes

towards that of a smaller particle (Figure 4). The effective size parameter of porous particles can be computed according to the equation, $X_{eq,p} = X_{eq} * (1 - p)^{1/3}$, where p is the porosity of the particle. Hence, our non-porous particles with $X_{eq} = 2.5$ have effective size parameters of 2.27, 2.10 and 1.84 for the three porosities 25%, 40% and 60% respectively.

Heterogeneous

Some comet particles may be a mixture of silicate and absorbing material on a small scale compared to wavelength. To simulate such particles, we introduce heterogeneity into our model particle by randomly replacing a fraction of the dipoles with a different refractive index from that of the parent particle. We start with a non-porous, homogeneous silicate sphere or tetrahedron with $X_{eq} = 2.5$ and gradually replace random single dipoles by carbon. In this fashion, we gradually vary the Si:C ratio from a pure silicate particle to a pure carbon particle. The resulting polarization curves are plotted in Figure 10.

In a heterogeneous sphere, the main change occurs at a phase angle $\leq 90^\circ$, where the strong negative polarization is converted to strong positive polarization with an inclusion of 25% carbon. With 40% carbon in the particle, the polarization curve resembles that of a pure carbon sphere of the same size. A homogeneous, non-porous silicate tetrahedron exhibits negative polarization at phase angles less than 60° and a positive maximum of polarization about 25%. The introduction of a small amount of carbon, about 570, is sufficient to suppress the negative branch. As the fraction of carbon increases, two maxima appear and the polarization is transformed to that of an absorbing particle. It is important to note, however, that intermediate Si : C ratios, such as 75 : 25, produce polarization curves that do not resemble either end member.

When inhomogeneities in a material occur on a scale small compared to the wavelength, it may be possible to define effective optical constants for the material (Bohren and Huffman, 1983). We

have tested whether effective optical constants can adequately represent the polarization by our porous and heterogeneous particles. We used the Bruggeman effective medium theory to compute effective refractive indices (these are listed in Table II). We compared the results from DDSCAT calculations with those of Mie calculations. In all cases, the polarization closely matched our results from the porous and heterogeneous particles (within 5%). Effective medium theory does not solve the problems inherent in using spheres, but can provide a useful method of computing effective refractive indices of porous and/or heterogeneous non-spherical particles.

Comparison with Previous Work.

Most previous investigations have been based either on spheres or on aggregates composed of spheres smaller than the wavelength of light. Here, we illustrate the problems associated with spheres and aggregates of spheres with a few examples. Mukai *et al.* (1987) used Mie theory to compute the linear polarization for a particle size distribution measured by the Halley Vega space probe. They systematically varied the refractive index, finding a fit to the comet polarization only for $m = 1.39 + 0.0352$, very different from the refractive indices of silicate and carbon particles that are known to be present in comets. Their study illustrates that the use of spheres can lead to rather different conclusions about the compositions of the particles, contrary to observations. They also confirm that integration over a broad size distribution of spheres leads to strong negative polarization for typical silicate refractive indices.

West (1991) clearly demonstrated the importance of monomer size in determining the polarization by an aggregate particle. He constructed two aggregates with the same equivalent volume, one composed of 170 spherical monomers and one composed of 8 spherical monomers having a radius r_m equal to half the volume equivalent radius of the aggregate (Type II). The Type I aggregates display Rayleigh polarization, while the Type II aggregates deviate from Rayleigh polarization

when the monomer size parameter $X_m > 1$, consistent with our results. Calculations by Kozasa *et al.* (1993) indicate that, porous aggregates composed of non porous spherical monomers in the Rayleigh regime produce the characteristic Rayleigh polarization. West and Smith (1991) concluded that aggregates composed of Rayleigh spheres could explain both the forward scattering (property of the aggregate) and the high linear polarization (property of the monomer) in Titan's haze. Thus, there are applications where the use of spheres is appropriate; in the case of Titan's haze, at least some of the polymers are likely to be composed of spheres (Clarke and Ferris 1997). For larger monomers, Giese *et al.* (1978) concluded from their microwave measurements of various large and fluffy aggregates ($X_{eq} \sim 20 - 30$) that optical properties of the aggregates are influenced by the optical properties of the individual constituent particles. They measured a strong positive polarization for their large and fluffy irregular absorbing particles similar to our model for large ($X_{eq} = 5$) carbon particles.

In contrast, the work by Mishchenko (1993) is more comparable to our results. He used the T-matrix method to compute the phase matrix for shape distributions of spheroids with $X_{eq} = 3.4$ and 9 and $m = 1.5 + 0.02i$. As the axial ratio of the spheroids increased, the polarization at intermediate phase angles changed from negative (characteristic of spheres) to positive, leaving a negative branch at $0 - 30^\circ$ phase. Thus, his results support our conclusions for the trends in polarization for non-spherical silicate particles in this size range.

The effect of roughness and porosity on the phase function and polarization was studied by Perrin and Sivan (1991) for silicate and carbon spheres with size parameters less than 1, 1.43, and 1.96. Spheres undergo major changes in polarization as the size parameter changes from 1.5 to 2.0 to 2.5 (Fig. 2), with strong negative polarization developing for both carbon and silicate spheres. Perrin and Sivan show that for $X_{c,r} = 1.96$ carbon spheres, both roughness and 60% porosity eliminate the negative polarization and produce strong positive polarization. In contrast,

our porous carbon spheres with $X_{eq} = 2.5$ retain their negative polarization, probably due to the somewhat larger size parameter.

Xing and Hanner (1997) have used DDSCAT to investigate the polarization for aggregates composed of spherical and tetrahedral monomers with $X_{eq} = 2.5$ and 5, similar to the particles studied in our work. Both the shape and size of the monomer and the structure of the aggregate influence the polarization. The polarization for their 10-monomer “touching” aggregates (porosity 60%) of carbon or silicate tetrahedral is intermediate between the polarization of the monomer and that of a single tetrahedron with equivalent volume size parameter equal to that of the aggregate. A mixture of carbon and silicate aggregates with monomer size $X_{eq} \sim 2.5$ produces a polarization curve with a small negative polarization branch resembling that of comets.

B. Phase Function

A secondary observable property of comets is their phase function. The observed phase function for comets has the general features of a steep rise from 60 to 30° scattering angle; relatively flat response for intermediate angles and an enhancement in the backscatter direction by a factor of 2 (defined as the ratio of the brightness at 180° to that at 1500). (Millis *et al.*, 1982; Ney and Merrill, 1976; Hanner and Newburn, 1986; Meech and Jewitt, 1987).

The influence of particle shape on the phase function is shown in Figure 11. Shape effects are manifested in the strength of the forward diffraction peak and the backscatter enhancement. A spherical particle exhibits the well known rainbows at intermediate scattering angles (60 - 120°); The silicate: sphere and cube have similar phase functions; both display structure at intermediate scattering angles (60 - 150°) and exhibit enhancement in the backscatter direction (Figure 1 la). other shapes have featureless, but steep phase functions at intermediate scattering angles and some backscatter enhancement. One sees in Table I [A] that the backscatter enhancement more closely

resembles that of the comets for size parameter $X_{eq} = 5$ rather than $X_{eq} = 2.5$. In Figure 11 b, carbon particles display relatively flat phase functions at intermediate scattering angles and, except for the flat brick (b), do not display backscatter enhancement.

Figures 12 and 13 illustrate the influence of porosity for particles with an initial volume equivalent size parameter of 2.5. The main effects of porosity for both the sphere and tetrahedron are stronger forward scattering and steeper phase function at scattering angles less than 90°. For a sphere, the introduction of porosity actually enhances the resonances at scattering angles larger than 60°, in both silicate and absorbing particles. Porosity does not introduce a backscatter enhancement for the carbon tetrahedron. Perrin and Sivan (1991) find that surface roughness causes enhanced backscatter for silicate spheres, $X_{eq} = 1.43$, whereas porosity does not. Their rough or porous carbon particles with $X_{eq} = 1.96$ have steeper phase functions than the corresponding smooth spheres.

The phase function for a two-component heterogeneous tetrahedron is shown in Figure 14. The change in the shape of the phase function is gradual. The backscatter enhancement does not completely disappear until the particle is about 40% carbon, in contrast to the smaller amount (5 - 10 %) of carbon required to suppress the negative linear polarization. Giese *et al.* (1978) found a slight enhancement in backscattering to be typical for rough or fluffy absorbing particles, with a range of size parameters 20 - 30. Our heterogeneous particle, with 25% carbon in the matrix, displays similar features as the rough and fluffy absorbing particles of Giese *et al.* (1978). The effective refractive index of our particle is (1.75, 0.27), not very different from that of the large rough and fluffy absorbing particles (1.65, 0.25). If our heterogeneous particle was about 15-20% porous, its refractive index might be almost the same as Giese *et al.* (1978) particles.

Therefore, we conclude that non-spherical predominantly silicate or “dirty” silicate particles, including rough or porous particles, with a characteristic dimension comparable to the wavelength

of light can produce the observed backscatter enhancement in comets. Carbon particles display a rather flat curve in the backscatter direction.

The dust in comets undoubtedly spans a size distribution of particles and aggregate particles. To illustrate the sensitivity of the phase function and polarization to particle size over the size range we studied, we computed these quantities for particles obeying a power law size distribution of the form $n(a)da \propto X_{eq}^{-\alpha}$, for tetrahedral particles over the range $1 \leq X_{eq} \leq 5$. We find that a fairly flat size distribution ($\alpha \leq 0.25$) is needed to generate both the negative linear polarization at phase angles less than 21° and maximum polarization of 40% near 90° . The phase function for this flat size distribution exhibits a steep rise in the forward direction and a slight enhancement in the backscatter direction (Figure 15).

C. Silicate Emission Feature

A number of comets exhibit an emission feature near $10 \mu\text{m}$ attributed to small silicate particles. The $10 \mu\text{m}$ spectra of P/Halley and several other comets display a broad maximum at $9.8 \mu\text{m}$ and a narrower peak at $11.2\text{--}11.3 \mu\text{m}$ (Fig. 1b; Hanner *et al.* 1994a,b and references therein). The $11.25 \mu\text{m}$ peak most likely arises from crystalline olivine; the good correspondence between the comet spectra and the measured emission spectrum of a crystalline olivine sample (Stephens and Russell 1979) is evident in Fig. 1b. The $9.8 \mu\text{m}$ maximum could be due either to amorphous or disordered silicate (Hanner *et al.* 1994a) or to a heterogeneous mixture of crystalline pyroxenes and hydrated silicate (Bregman *et al.* 1987; Sandford and Walker 1985). Chondritic aggregate IDPs containing glassy silicates show spectra similar to the cometary features, lending support to the amorphous silicate interpretation (Bradley *et al.* 1992).

Features produced by resonances in the optical constants, such as the olivine peak, are extremely sensitive to particle shape (Bohren and Huffman 1983). Even when the particle dimensions are much

less than the wavelength, shape effects are important, a point that has often been glossed over in the literature. We have investigated the effect of shape on the olivine feature for particles having physical dimensions similar to the particles with $X_{eq} = 2.5 - 5$ at wavelength $0.6 \mu\text{m}$.

Olivine is an anisotropic crystal, with different optical constants along the three principal axes. We have used the refractive indices measured in the 3 orthogonal directions by Steyer (1974) for a polished sample of forsterite (Mg_2SiO_4). Computations were run separately for each principal axis and the resulting Q_{abs} were averaged to simulate randomly oriented particles. The thermal emission from a particle at any wavelength is proportional to the product of the emissivity and the Planck function for the appropriate grain temperature. By Kirchoff's law, the emissivity is equivalent to the absorption efficiency factor, Q_{abs} (Bohren and Huffman 1983).

Shape and anisotropic effects on the absorption efficiency factor, Q_{abs} , are illustrated in Figure 16. Figure 16a depicts the emissivity for a sphere with $X_{eq} = 0.4$ at $9.8 \mu\text{m}$. Twin peaks are visible at 10.8 and $11.0 \mu\text{m}$, corresponding to $E \parallel b$ and $E \parallel a$; a smaller peak due to $E \parallel c$ occurs at $\lambda \leq 10 \mu\text{m}$. *There is 1 peak at all at $11.2 \mu\text{m}$ in a single sphere!* In contrast, tetrahedral particles (Fig. 16b) generate $E \parallel a$ and $E \parallel b$ peaks at $11.2 - 11.3 \mu\text{m}$, leading to a strong $11.25 \mu\text{m}$ peak in the average, and a weaker $E \parallel c$ peak at $10.0 \mu\text{m}$. This spectrum is very similar to the measured emissivity of crystalline forsterite. As the size parameter is varied from 0.03 to 0.5, the amplitude of the peak increases and the full width at half maximum decreases; the peak remains at the same wavelength. Figure 16c presents the emissivity for a brick (axial ratios 5:3:1). Here, the peaks break into 3 components, reflecting the differing axial dimensions, but the strongest peak is near $11.3 \mu\text{m}$. Employing the analytical expressions for a disk or needle from Bohren and Huffman (1983) yielded a peak at $11.5 - 11.6 \mu\text{m}$. A continuous distribution of ellipsoids in the Rayleigh limit (Bohren and Huffman, 1983) predicts a peak at ~ 11.411111 (Hanner *et al.* 1994a).

To investigate the effect of aggregate structure, we created two- and five-monomer aggregates

consisting of spheres or tetrahedra with $X_{eq} = 0.3$ - 0.4 at $10 \mu\text{m}$ for the monomers. In the case of the tetrahedra, we created both open (“fluffy”) and compact aggregates by controlling the overlap of the individual tetrahedra (10% overlap for the fluffy aggregates and 33% for the compact aggregates). A fluffy aggregate is illustrated in Figure 17. While the basic characteristics of the unit particles are maintained, one sees in Figure 18 that, a weak shoulder at $11.2 \mu\text{m}$ develops for the aggregates of spheres. Aggregates of tetrahedral monomers exhibit emission features similar to those of the individual monomers (Figure 19). There are minor differences in width and peak wavelength between the fluffy and compact aggregates.

Hence, generation of a peak near $11.25 \mu\text{m}$ in crystalline forsterite requires non-spherical particles that are not extremely elongated, and/or aggregates of such particles. Contrary to popular misconception, shape effects are important even when the particles are small compared to the wavelength.

Shape effects are less dramatic for glassy, or amorphous, silicates. Figure 20 compares the emission feature for a sphere and a tetrahedron using the refractive indices for a disordered silicate with the composition of forsterite (Kratschmer and Huffman 1979). The feature for the tetrahedron is of comparable strength, but somewhat broader than that of a sphere. Figure 21 shows the effect of combining varying fractions of crystalline and amorphous tetrahedral particles. A component of 20% crystalline particles produces maxima of comparable strength at 10 and $11.25 \mu\text{m}$, similar to the comet spectra.

Small silicate grains also produce spectral features in the 16 - $30 \mu\text{m}$ region. A 16 - $40 \mu\text{m}$ spectrum of comet Hale-Bopp was obtained with the Infrared Space Observatory (Figure 4 in Crovisier et al. 1997). Several broad peaks are present in the spectrum which correlate with the positions of olivine features in laboratory spectra; the strongest of these occur at 19.3 and $23.7 \mu\text{m}$. Our calculations for a tetrahedral particle of crystalline forsterite with $X_{eq} = 0.5$ at $20 \mu\text{m}$

are plotted in Figure 22. The peak at, $19.0 - 19.5 \mu\text{m}$ matches that of the comet; the peak at $23.4 \mu\text{m}$ is also similar to the cometary feature, but occurs at slightly shorter wavelength.

IV. CONCLUSIONS

We have used the DDA method to compute the scattering by particles of various shapes, in order to interpret two cometary observations that are sensitive to particle shape: negative linear polarization at small phase angles at visual wavelengths and a peak at $11.2 \mu\text{m}$ in the thermal emission due to crystalline olivine.

Our main result is that compact, non-spherical silicate particles with equivalent volume size parameter $X_{eq} \sim 2.5$ can have polarization curves that qualitatively resemble those of comets, with negative polarization at small phase angles and maximum positive polarization $\sim 20\%$ centered near 90° . Carbon particles with $X_{eq} = 2.5 - 5$ generally have strong positive polarization. However, the polarization is very low at small phase angles, so that a macroscopic mixture of carbon and silicate particles in this size range could yield the small net negative polarization typical of comets.

Inhomogeneity in the form of porosity and heterogeneous composition influence both the negative branch of polarization and the phase function. The effect of porosity in silicate particles is to suppress the negative polarization and increase the positive polarization; a very porous particle will resemble a smaller particle, tending toward high positive polarization near 90° . Even a small fraction of carbon ($\sim 5\%$) in the silicate matrix suppresses the negative polarization. Thus, mixtures of silicate and carbonaceous material on a scale small compared to the wavelength are not a good model for cometary dust.

We found that calculations using effective refractive indices computed by the Bruggeman effective medium theory accurately predicted the polarization and phase function for our porous and heterogeneous particles. However, effective medium theory alone does not circumvent the

resonances inherent in using spheres.

Not only do spheres exhibit resonances not present in tile scattering by non-spheres, but they do not even give a qualitatively correct picture of the scattering by compact non-spherical particles. This fact is particularly important for studies of aggregate particles. Since the polarization produced by an aggregate is influenced by the polarization properties of the constituent monomers, aggregates composed of spheres will not generate polarization typical of aggregates composed of non-spherical particles. Furthermore, monomers much smaller than the wavelength will give rise to Rayleigh polarization, regardless of the dimensions of the aggregate, unless the aggregate has a very compact, non-porous structure.

We examined the $11.2 \mu\text{m}$ emission feature of crystalline olivine for several particle shapes, including small aggregates, using particles with physical dimensions similar to the particles studied at visual wavelengths ($X_{eq} \sim 0.3$ at $9.8 \mu\text{m}$). Our results clearly illustrate how particle shape governs the wavelength of an emission feature or a resonance in the optical constants, even when the particle dimensions are small compared to the wavelength. The peak near $11.2 \mu\text{m}$ in naturally occurring forsterite (Mg_2SiO_4) measured in the laboratory and the $11.2 \mu\text{m}$ peak seen in comets can be matched with shapes such as tetrahedra or moderately elongated bricks. Extreme shapes, such as disks or needles, appear to be ruled out. Spheres produce twin peaks at 10.8 and $11.0 \mu\text{m}$; there is no peak at all near $11.2 \mu\text{m}$. Therefore, spheres are not appropriate to use for modeling the $11.2 \mu\text{m}$ emission peak in comets, a fact which has not always been acknowledged in the literature. Small aggregates of spheres or tetrahedra exhibit emission features similar to those of the single constituent particles. The recently observed 19 and $23 \mu\text{m}$ features in the spectrum of comet Hale-Bopp can also be matched with the calculated spectra of tetrahedra, using refractive indices of forsterite.

Shape effects play only a minor role in the emission feature produced by amorphous or glassy

silicate particles. A component of 20 % crystalline olivine particles and 80 % disordered olivine produce maxima of comparable strength at 10 and 11.2 μm , similar to the spectra of P/Halley and several other comets.

Thus, non-spherical silicate particles of size comparable to the wavelength or aggregates of such particles can generate both the negative linear polarization seen at small phase angles in cornets and the silicate emission feature seen in the 10 μm spectra of comets.

We have illustrated an approach to determining the optical properties of non-spherical particles of size comparable to the wavelength. We also provide a framework to model porosity and heterogeneity in particles. Some basic scattering parameters have been tabulated for each case studied, in addition to our discussion of the polarization properties. Other work that follows naturally from our study is the influence of monomer properties on the scattering by an aggregate (Xing and Hanner 1997) Our results are widely applicable to cases where the particle size is comparable to the wavelength, such as the Shoemaker-Levy 9 debris in Jupiter's atmosphere and dusty planetary rings.

Acknowledgements.

This research was performed at the Jet Propulsion Laboratory, California Institute of Technology under contract with NASA. The DDSCAT numerical code (version 4a) was kindly provided by Dr. B. Draine. P. A. Y.-F. is grateful to the Supercomputing groups at both JPL and GSFC for their help and timely assistance in ensuring successful execution of the DDSCAT algorithm on the Cray YMP. We thank Dr. R.A. West for his helpful comments. The Cray supercomputers used in this investigation were provided by funding from NASA offices of Mission to Planet Earth, Aeronautics, and Space Science.

REFERENCES

- Bohren, C. I? and D. R. Huffman 1983. Absorption and *Scattering Of Light by Small Particles*, Wiley, New York.
- Bradley, J. P., H. J. Humecki and M. S. Germani 1992. Combined infrared and analytical electron-microscope studies of interplanetary dust particles. *Astrophys. J.*, 394, 643-651.
- Bregman, J. D., H. Campins, F. C. Witterborn, D. H. Wooden, D. H. Rank, L. J. Allamandola, M. Cohen and A. G.G.M. Tielens 1987. Airborne and groundbased spectrophotometry of comet P/Halley from 5-13 micrometers. *Astron. Astrophys.*, 187, 616 - 620.
- Brownlee, D. E. 1985. Cosmic dust - collection and research. *Ann. Rev. Earth Plan. Sot.*, 13, 147 - 173.
- Campins, H. and E. Ryan 1989. The identification of crystalline olivine in cometary silicates. *Astrophys. J.*, 341, 1059- 1066.
- Clarke, D. W. and J. P. Ferris. 1997. Titan haze: structure and properties of cyanoacetylene-acetylene photopolymers. *Icarus*, 127, 158-172.
- Crovisier, J., K. Leech, D. Bockelee-Morvan, T.Y. Brooke, M.S. Hanner, B. Altieri, H.U. Keller and E. Lellouch 1997. The spectrum of comet Iisele-Iopp (C/ 1995 O1) observed with the Infrared Space observatory at 2.9 astronomical units from the sun. *Science*, 275, 1904- 1907.
- Dollfus, A., I'. Bastien, J.F. La Borgne, A, C. Levasseur-Regourd and 'i'. Mukai 1988. optical polarimetry of P/Halley - Synthesis of the measurements in the continuum. *Astron. Astrophys.*, 206, 348-356.
- Draine, B. T. 1988. The discrete dipole approximation and its application to interstellar graphite grains. *Astrophys. J.*, 333, 848-872.

- Draine, B. T. and P. J. Flatau 1994. Discrete-dipole approximation for scattering calculations. *J. opt. sm.*, 11, 1491-1499.
- Edoh, O. 1983. Optical properties of carbon from the far infrared to the far ultraviolet. *Ph. D. Dissertation*, University of Arizona.
- Giese, R. H., K. Weiss, R. H. Zerull and T. One. 1978. Large fluffy particles: a possible explanation of the optical properties of interplanetary dust. *Astron. Astrophys.*, 65, 265-272.
- Goodman, J. J., B. T. Draine and P. J. Flatau 1990. Application of fast-Fourier transform techniques to the discrete dipole approximation. *Opt. Lett.*, 16, 1198-1200.
- Hanner, M. S. 1983. The nature of cometary dust from remote sensing. In *Cometary Exploration*, Ed. T. I. Gombosi, vol. 2, 1-22.
- Hanner, M. S., E. Tedesco, A. T. Tokunaga, G. J. Veeder, D. F. Lester, F. C. Witterborn, J. D. Bregman, J. Gradie and L. Lebofsky 1985. The dust coma of periodic comet Churyumov-Gerasimenko (1982 VIII). *Icarus*, 64, 11-19.
- Hanner, M. S. and R. I. Newburn 1986. Infrared photometry of comet Wilson (1986) at two epochs. *Astron. J.*, 97, 254-261.
- Hanner, M. S., D. K. Lynch and R. W. Russell 1994a. The 8-13 micron spectra of comets and the composition of silicate grains. *Astrophys. J.*, 425, 274-285.
- Hanner, M. S., J. A. Hackwell, R. W. Russell and D. K. Lynch 1994b. Silicate emission feature in the spectrum of comet Mueller 1993a. *Icarus*, 112, 490-495.
- Kissel, J. et al., 1986. Composition of comet Halley dust particles from Vega observations. *Nature*, 321, 280-282.
- Kozasa, T., J. Blum and T. Mukai 1992. Optical properties of dust aggregates. I. Wavelength

- dependence. *Astron. Astrophys.*, 263, 423-432.
- Kozasa, T., J. Blum, H. Okamoto and T. Mukai 1993. Optical properties of dust, aggregates. II. Angular dependence of scattered light. *Astron. Astrophys.*, 276, 278-288.
- Kratschmer, W. and D. R. Huffman 1979. Infrared extinction of heavy ion irradiated and amorphous olivine with application to interstellar dust. *Astrophys. Space Sci.* 61, 195.
- Levasseur-Regourd, A. C., Hadamcik, E. and J. B. Renard 1996. Evidence for two classes of comets from their polarimetric properties at large phase angles. *Astron. Astrophys.*, 313, 327-333.
- Meech, K. and D. Jewitt 1987. Observations of comet P/Halley at minimum phase angle. *Astron. Astrophys.*, 187, 585-593.
- Minis, R. L., M. F. A'Hearn and D. I. Thompson 1982. Narrowband photometry of comet P/Stephan-Oterma and the backscattering properties of cometary grains. *Astron. J.*, 87, 1310-1317.
- Mishchenko, M. 1993. Light scattering by size-shape distributions of randomly oriented axially symmetric particles of a size comparable to a wavelength. *Appl. Opt.*, 32, No. 24, 4652-4666.
- Mukai, T., S. Mukai, and S. Kikuchi 1987. Complex refractive index of grain material deduced from the visible polarimetry of Comet P/Halley. *Astron. Astrophys.*, 187, 650-652.
- Ney, E. P. and K. M. Merrill 1976. Comet West and the scattering function of cometary dust. *Science*, 194, 1051-1053.
- Perrin, J. M. and J. P. Sivan 1991. Scattering and polarization of light by rough and porous interstellar grains. *Astron. Astrophys.*, 247, 497-504.
- Purcell, E. M. and C. R. Pennypacker 1973. Scattering and absorption of light by nonspherical

dielectric grains. *Astrophys. J.*, **186**, 705–714.

Sandford, S. and R. Walker 1985. Laboratory infrared transmission spectra of individual interplanetary dust particles. *Astrophys. J.*, **291**, 838–851.

Stephens, J. and R.W. Russell 1979. Emission and extinction of ground and vapor-condensed silicates from 4 to 14 microns and the 10 micron silicate feature. *Astrophys. J.*, **228**, 780–786.

Steyer, T. R. 1974. Infrared Optical Properties of Some Solids of Possible Interest in Astronomy and Atmospheric Physics. Ph. D. *Dissertation*, University of Arizona.

van de Hulst, H. C. 1957. *Light Scattering by Small Particles*, J. Wiley and Sons, New York.

West, R. A. 1991. Optical properties of aggregate particles whose outer diameter is comparable to the wavelength. *App. Opt.*, **30**, No. 36, 5316–5324.

West, R. A. and P. H. Smith 1991. Evidence for aggregate particles in the atmospheres of Titan and Jupiter. *Icarus*, **90**, 330–333.

Xing, Z. and M. S. Hanner. 1997. Light scattering by aggregate particles. *Astron. Astrophys.*, *In Press*.

Zerull, R. H., B. Gustafson, K. Schulz and E. Thiele-Corbach 1993. Scattering by aggregates with and without an absorbing mantle: microwave analog experiments. *Appl. Opt.*, **32**, No. 21, 4088–4100.

FIGURE CAPTIONS

Figure 1. (a). Composite polarization curve vs. phase angle from many cometary observations, (Levasseur-Regourd *et al.*, 1996). (b). Thermal emission of comets Mueller (open circles) (Hanner *et al.*, 1994b) and Halley (solid line)(Campins and Ryan, 1989), compared with the emission for crystalline olivine (filled circles) (Stephens and Russell 1979).

Figure 2. Polarization curves vs. phase angle for spheres, $X_{eq} = 1 - 5$. (a). Silicate (b). Carbon

Figure 3. Polarization curves vs. phase angle for brick, having an aspect ratio of its principal axes (5:5:1), $X_{eq} = 1 - 5$. (a). Silicate (b). Carbon

Figure 4. Polarization vs. phase angle for tetrahedral, $X_{eq} = 1 - 5$. (a). Silicate (b). Carbon

Figure 5. A negative branch of polarization first appears in a silicate tetrahedron at intermediate phase angles and moves to smaller phase angles as X_{eq} is increased from 2 to 2.5.

Figure 6. Polarization vs. phase angle for six different particle shapes, all having $X_{eq} = 2.5$. (a). Silicate particles exhibit negative linear polarization at low phase angles. (b). Carbon cylinder and hexagonal prism display negative branch of linear polarization.

Figure 7. Polarization vs. phase angle for the six particles as in Fig. (6), but for $X_{eq} = 5$. (a). Silicate (b). Carbon

Figure 8. Effect of porosity on the polarization curves of spheres having initial $X_{eq} = 2.5$. (a). Silicate (b). Carbon

Figure 9. Effect of porosity on the polarization curves of tetrahedra having initial $X_{eq} = 2.5$. (a). Silicate: negative linear polarization is suppressed as porosity is increased (b). Carbon

tetrahedron displays no negative polarization and none is introduced as porosity is increased.

Figure 10. Polarization vs. phase angle for silicate : carbon mixture with $X_{eq} = 2.5$. Negative linear polarization decreases with increasing carbon content. (a). Sphere (b). Tetrahedron

Figure 11. Phase function vs. scattering angle as function of shape. (a). Silicate particles with $X_{eq} = 2.5$. (b). Similar curves for carbon particles.

Figure 12. Effect of porosity on phase function vs. scattering angle for initial $X_{eq} = 2.5$. (a). Porous silicate sphere. (b). Porous carbon sphere

Figure 13. Corresponding phase functions for porous tetrahedral.

Figure 14. Phase function vs. scattering angle for heterogeneous tetrahedron at $X_{eq} = 2.5$.

Figure 15. (a). Polarization for power law size distributions of tetrahedra, $n(a) \sim a^{-\beta}$. An exponent between 0 and 0.25 yields small negative linear polarization at low phase angles and moderate positive polarization, similar to the observed polarization in comets. (b) Phase function corresponding to the power law size distributions in (a).

Figure 16. The silicate feature in the thermal emission spectrum of a crystalline forsterite particle. Since forsterite is anisotropic, Q_{abs} corresponding to each of the three principal axes is shown: (a). sphere, $X_{eq} = 0.4$ at $\lambda = 9.5 \mu\text{m}$; (b). tetrahedron, $X_{eq} = 0.3$ at $\lambda = 9.6 \mu\text{m}$ and (c): brick with aspect ratio 5:3:1, $X_{eq} = 0.3$ at $\lambda = 9.6 \mu\text{m}$.

Figure 17. .4 visualization of a fluffy aggregate composed of five tetrahedral monomers. The individual dipoles are depicted as spheres; the envelope of each monomer is a tetrahedron; the overall envelope of tile aggregate is random, with size and porosity varying as a function of orientation.

Figure 18. The silicate feature in an aggregate composed of five spherical monomers exhibits

twin peaks at $10.8 \mu\text{m}$ and $11.0 \mu\text{m}$ and two small, distinct shoulders at $10.5 \mu\text{m}$ and $11.2 \mu\text{m}$.

Figure 19. Silicate feature in aggregates of 2 and 5 tetrahedra. Q_{abs} is averaged over the three orthogonal components.

Figure 20. Absorption efficiency *vs.* wavelength for disordered olivine sphere (filled circles), disordered olivine tetrahedron (diamonds) and crystalline olivine tetrahedron (asterisks).

Figure 21. Absorption efficiency *vs.* wavelength for a disordered olivine tetrahedron (diamonds) and varying fraction of crystalline olivine.

Figure 22. Absorption efficiency *vs.* wavelength from 18 to $24 \mu\text{m}$ for a crystalline forsterite tetrahedron, with effective radius $a = 1.51 \mu\text{m}$ (asterisks) and $a = 0.477 \mu\text{m}$ (diamonds). The peaks closely match those seen in comet Hale-Bopp (Crovisier *et al.* 1997).

Table IA Matrix of Cases Studied				
Monomer Shape	Eq. Vol. Size Parameter (X_{eq})	Principal Axes Aspect Ratio	Monomer Composition*	
Sphere	0.5- 5.0	1:1:1	s, c, p, h	
Brick (a)	2.5, 5.0	5:2:1	s, c	
Brick (b)	0.5- 5.0	5:5:1	s, c, p, h	
Cube	2.5, 5.0	1:1:1	s, c	
Cylinder	2.5, 5.0	1:3	s, c	
Hexagon	2.5, 5.0	1:3	s, c	
Tetrahedron	0.5- 5.0	1:1:1	s, c, p, h	

*(s,c,p,h) stand for silicate, carbon, porous and heterogeneous.

Effectiv Particle Composition		Refractive Indices Particle Composition	
	n_r, n_i		n_r, n_i
silicate	1.65, 0.00	carbon	1.88, 0.71
<i>Porous silicate</i>		<i>Heterogeneous, Si:C</i>	
0 %	1.65, 0.00	100:00	1.65, 0.00
25 %	1.48, 0.00	95:05	1.66, 0.03
40 %	1.38, 0.00	90:10	1.68, 0.07
60 %	1.25, 0.00	75:25	1.72, 0.17
<i>Porous carbon</i>		60:40	1.75, 0.27
0 %	.88, 0.71	40:60	1.79, 0.42
25 %	.65, 0.53	25:75	1.82, 0.52
40 %	.51, 0.41	10:90	1.86, 0.63
60 %	.34, 0.24	00:100	1.88, 0.71

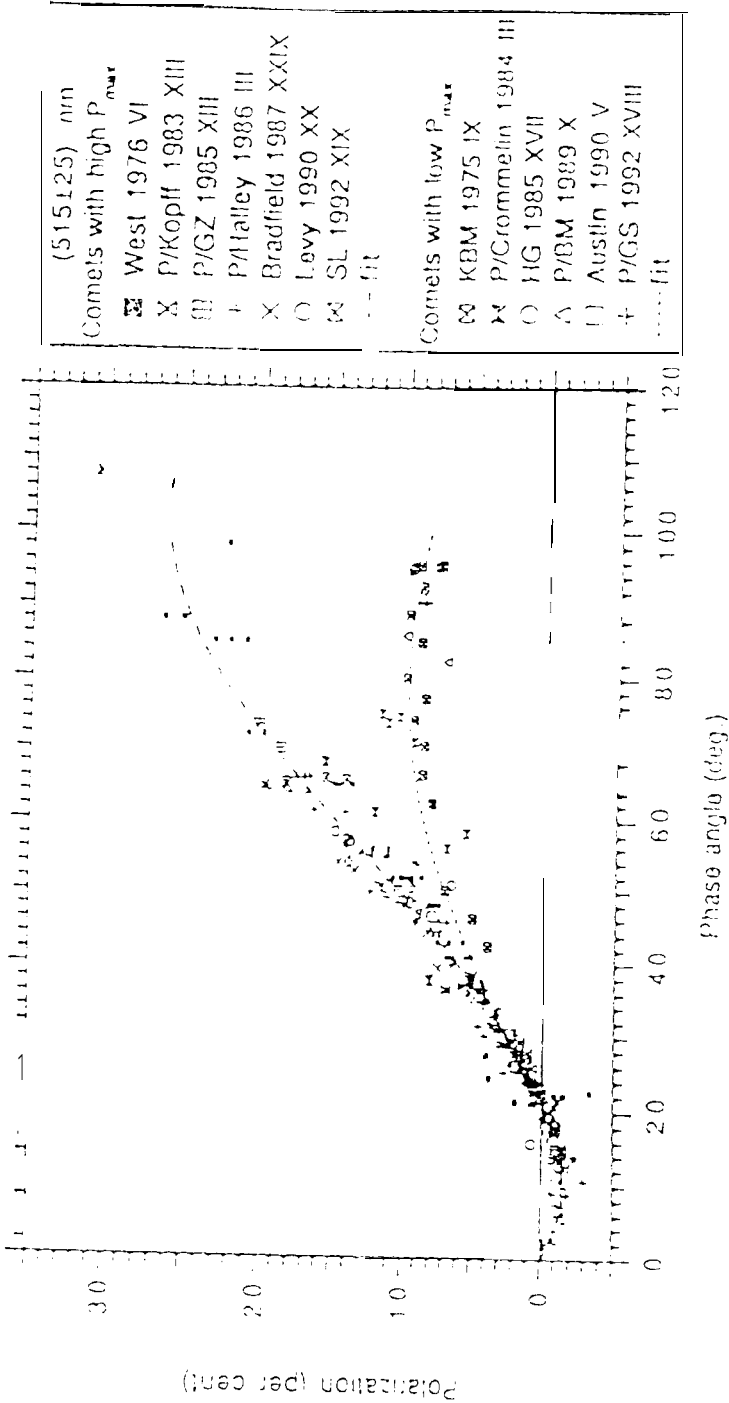
Table 113

Table 11A
Optical Properties of Homogeneous Particles

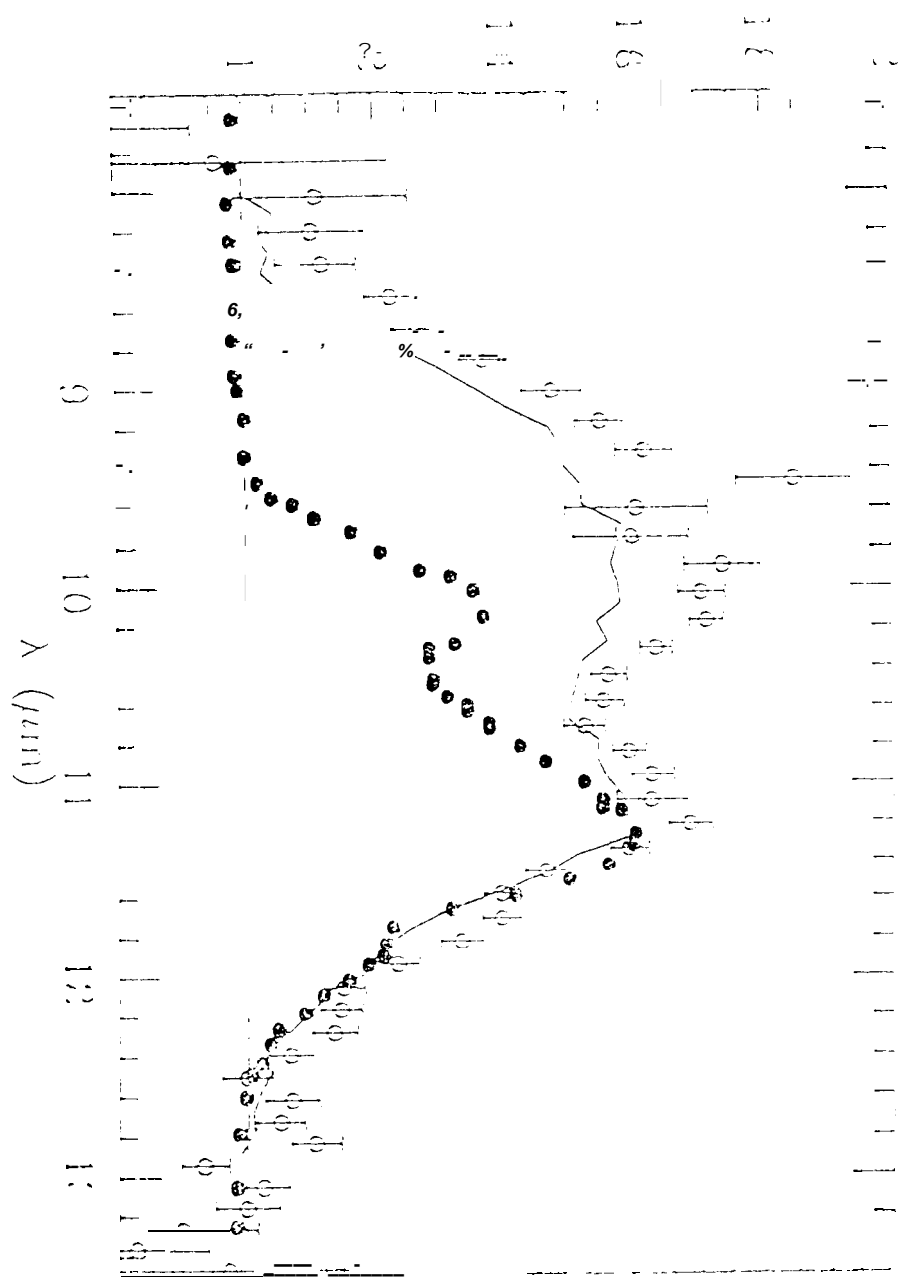
λ	Shape	Dipoles	Q_{sca}	Q_{abs}	\bar{w}_0	g	$P^{II}(0)$	$P^{II}(180)$	$P^{II}(180)/P^{II}(150)$
<i>Silicate</i>									
Sphere	1.0	4224	0.36	0.00	1.00	0.21	2.30	0.84	1.08
	1.5	4224	1.31	0.00	1.00	0.54	3.88	0.10	1.02
	1.75	4224	2.31	0.00	1.00	0.60	4.40	0.08	1.51
	2.0	4224	2.77	0.00	1.00	0.57	4.87	0.21	1.28
	2.5	4224	4.09	0.00	1.00	0.68	8.13	0.09	1.26
	3.0	4224	4.07	0.00	1.00	O.M	9.79	0.32	1.38
	5.0	33,552	2.39	0.00	1.00	0.48	18.76	1.83	2.75
Brick a	2.5	3332	3.29	0.00	1.00	0.70	9.60	0.10	1.04
	5.0	21632	4.82	0.00	1.00	0.76	33.76	0.22	2.27
Brick b	1.0	5400	0.33	0.00	1.00	0.29	2.84	0.61	0.22
	1.5	5400	1.18	0.00	1.00	0.49	4.53	0.29	1.03
	2.0	5400	2.20	0.00	1.00	0.63	7.16	0.17	1.25
	2.5	3125	3.14	0.00	1.00	0.70	10.29	0.18	1.53
	3.0	5400	3.74	0.00	1.00	0.75	14.52	0.09	1.15
	5.0	43,200	4.57	0.00	1.00	0.79	39.21	0.21	1.82
cube	2.5	3375	3.90	0.00	1.00	0.68	7.98	0.09	1.02
	5.0	64,000	2.59	0.00	1.00	0.47	17.66	0.72	1.25
Cylinder	2.5	2430	3.53	0.00	1.00	0.69	9.13	0.14	1.21
	5.0	20,916	4.67	0.00	1.00	0.74	31.36	0.24	1.79
Hexagon	2.5	1792	3.41	0.00	1.00	0.72	9.97	0.07	1.22
	5.0	43,000	3.95	0.00	1.00	0.61	26.55	0.38	2.11
Tetrahedron	1.0	3172	0.36	0.00	1.00	0.22	2.42	0.80	1.07
	1.5	3172	1.24	0.00	1.00	0.50	4.03	0.23	1.03
	2.0	3850	2.62	0.00	1.00	0.61	5.60	0.20	1.23
	2.05	2578	2.71	0.00	1.00	0.61	5.79	0.20	1.24
	2.10	2578	2.78	0.00	1.00	0.61	6.00	0.20	1.25
	2.15	2578	2.86	0.00	1.00	0.62	6.25	0.20	1.27
	2.20	2578	2.94	0.00	1.00	0.63	6.53	0.19	1.29
	2.25	2578	3.03	0.00	1.00	0.64	6.84	0.18	1.31
	2.50	3850	3.65	0.00	1.00	0.68	8.46	0.15	1.51
	3.0	3850	4.11	0.00	1.00	0.67	10.35	0.17	1.43
	5.0	20,688	3.22	0.00	1.00	0.52	19.79	0.21	1.14
<i>Carbon</i>									
Sphere	1.0	4224	0.70	1.43	0.33	0.24	2.42	0.74	1.07
	1.5	4224	1.21	1.62	0.43	0.50	4.01	0.10	0.72
	1.75	4224	1.30	1.65	0.44	0.60	5.30	0.03	0.63
	2.0	4224	1.36	1.66	0.45	0.66	6.73	0.14	1.43
	2.5	4224	1.35	1.59	0.46	0.72	9.86	0.15	0.97
	3.0	4224	1.33	1.53	0.46	0.76	13.59	0.08	0.92
	5.0	33,552	1.30	1.33	0.49	0.82	31.18	0.07	0.65
Brick a	2.5	2730	1.65	1.86	0.47	0.72	12.07	0.12	0.98
	5.0	21632	1.76	1.71	0.54	0.81	41.93	0.07	0.69
Brick b	1.0	5400	0.63	1.56	0.29	0.32	2.97	0.51	1.01
	1.5	5400	1.17	1.77	0.10	0.53	5.39	0.31	1.06
	2.0	5400	1.55	1.91	0.45	0.65	8.90	0.22	1.14
	2.5	5400	1.78	1.97	0.17	0.72	13.26	0.20	1.47
	3.0	5-100	1.91	1.97	0.49	0.77	18.56	0.19	1.67
	5.0	43,200	2.10	1.85	0.53	0.83	46.66	0.05	0.72
Cube	2.5	4913	1.38	1.65	0.45	0.72	10.26	0.1-1	0.89
	5.0	64,000	1.38	1.43	0.19	0.81	34.04	0.01	0.12
Cylinder	2.5	3920	1.61	1.82	0.47	0.71	11.73	0.09	0.86
	5.0	38,80S	1.48	1.52	0.49	0.82	36.66	0.16	1.36
Hexagon	2.5	2112	1.67	1.89	0.47	0.71	12.30	0.10	0.90
	5.0	43,008	1.48	1.52	0.49	0.82	36.77	0.15	1.28
Tetrahedron	1.0	3172	0.78	1.55	0.30	0.26	2.57	0.69	1.05
	1.5	3172	1.17	1.79	0.10	0.54	4.59	0.13	0.88
	2.0	3172	1.38	1.84	0.13	0.66	7.62	0.17	1.10
	2.50	3850	1.44	1.80	0.41	0.72	11.28	0.12	0.87
	3.0	3850	1.47	1.77	0.45	0.76	15.70	0.11	0.90
	5.0	25,448	1.57	1.63	0.49	0.82	38.38	0.09	0.93

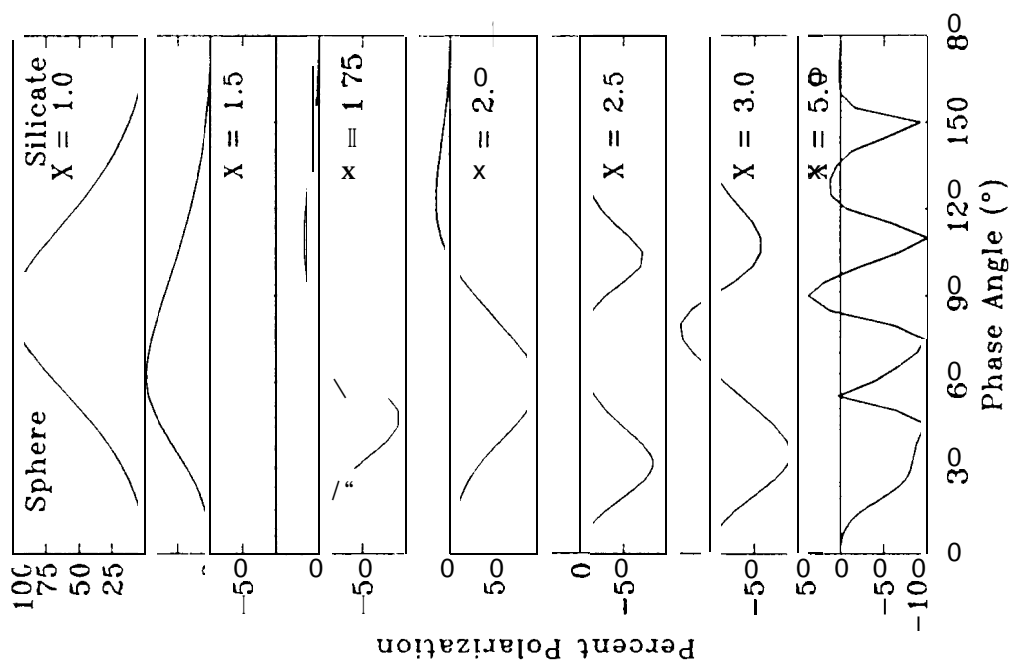
Table IIB
Optical Properties of Heterogeneous Particles; $X_{eq} = 2.5$

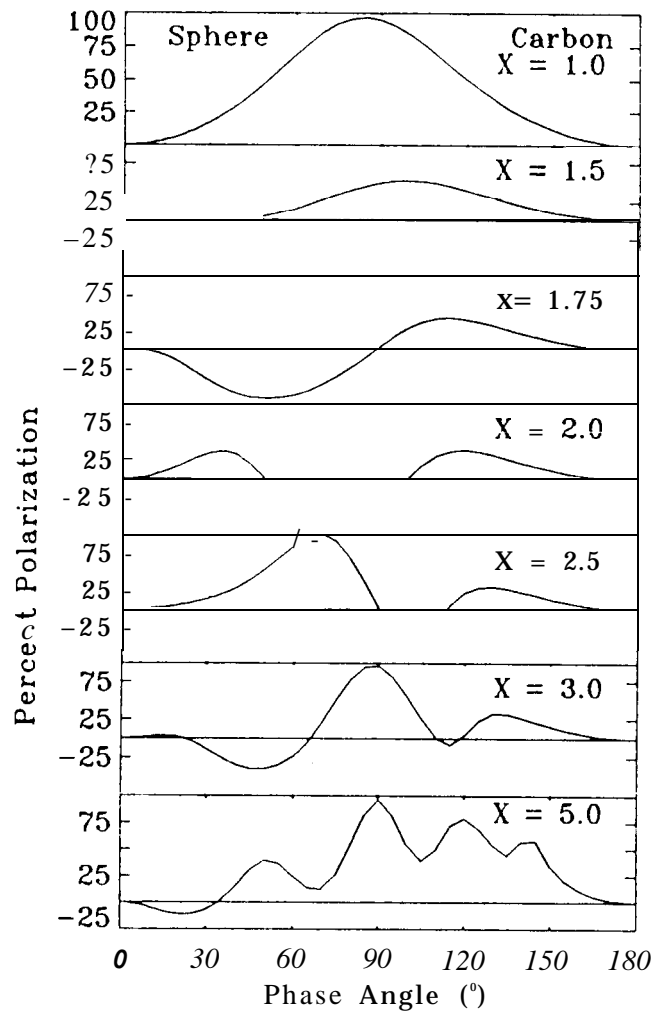
Shape	Dipoles	Q_{sca}	Q_{abs}	ω_0	g	$P^{II}(0)$	$P^{II}(180)$	$P^{II}(180)/P^{II}(150)$
<i>Silicate</i>								
<i>Porosity</i>								
Sphere								
0	3695	4.09	0.00	1.00	0.68	8.13	0.09	1.25
25	2758	3.50	0.00	1.00	0.74	9.25	0.08	0.64
40	2264	3.06	0.00	1.00	0.77	10.10	0.07	1.78
60	1455	2.26	0.00	1.00	0.82	12.72	0.06	2.73
Tetrahedron								
0	3850	3.65	0.00	1.00	0.68	8.46	0.15	1.51
25	2882	3.13	0.00	1.00	0.74	9.88	0.11	1.39
40	2315	2.72	0.00	1.00	0.77	11.16	0.08	1.30
60	1567	2.10	0.00	1.00	0.80	13.53	0.07	1.15
<i>Carbon</i>								
Sphere								
0	3716	2.95	1.59	0.46	0.72	9.89	0.15	0.96
25	2758	3.44	1.85	0.46	0.77	11.53	0.04	0.58
40	2264	3.73	2.00	0.46	0.80	12.60	0.03	0.59
60	1455	4.24	2.25	0.47	0.84	15.13	0.54	1.69
Tetrahedron								
0	3850	3.24	1.80	0.44	0.72	11.28	0.12	0.87
25	2882	3.66	2.03	0.80	0.44	12.92	0.08	0.90
40	2315	3.95	2.17	0.82	0.45	14.13	0.07	0.97
60	1567	4.24	2.33	0.82	0.45	16.46	0.05	0.99
<i>2-component</i>								
Si:C								
Sphere								
100:00	3695	4.09	0.00	1.00	0.68	8.13	0.09	1.25
95:05	3716	3.57	0.4'2	0.89	0.70	8.23	0.04	0.89
90:10	3716	3.13	0.74	0.81	0.72	8.43	0.01	0.32
75:25	3716	2.30	1.22	0.65	0.73	8.82	0.02	0.47
60:40	3716	1.87	1.43	0.57	0.73	9.22	0.06	0.85
40:60	3716	1.58	1.54	0.50	0.73	9.61	0.11	1.02
25:75	3716	1.44	1.58	0.48	0.73	9.80	0.13	1.02
10:90	3716	1.37	1.59	0.46	0.73	9.89	0.14	0.99
05:95	3716	1.37	1.59	0.46	0.72	9.89	0.15	0.98
00:100	3716	1.36	1.59	0.46	0.72	9.89	0.15	0.96
Tetrahedron								
100:00	3850	3.65	0.00	1.00	0.68	8.46	0.15	1.51
95:05	3850	3.29	0.39	0.89	0.70	8.75	0.12	1.46
90:10	3850	3.00	0.68	0.81	0.70	9.01	0.11	1.4'2
75:25	3850	2.27	1.27	0.64	0.72	9.71	0.0s	1.15
60:40	3850	1.92	1.51	0.56	0.73	10.02	0.08	0.99
40:60	3850	1.62	1.69	0.49	0.73	10.77	0.09	0.9-1
25:75	3850	1.52	1.75	0.46	0.73	11.04	0.10	0.89
10:90	3850	1.45	1.79	0.45	0.72	11.21	0.11	0.89
05:95	3850	1.44	1.80	0.45	0.72	11.27	0.11	0.88
00:100	3850	1.44	1.80	(0.44	0.72	11.28	0.12	0.87

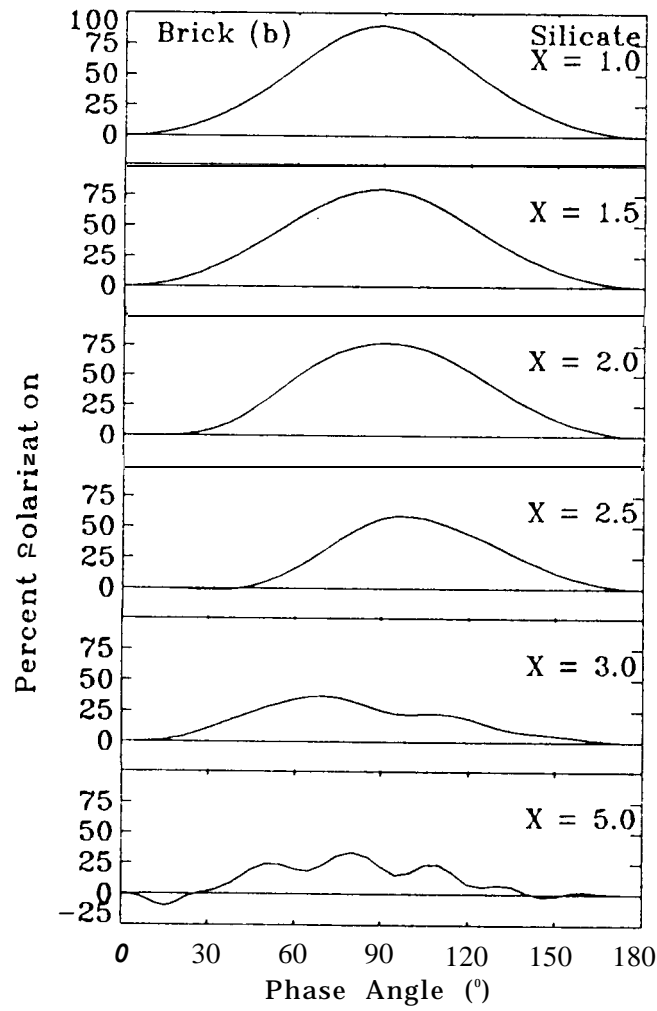


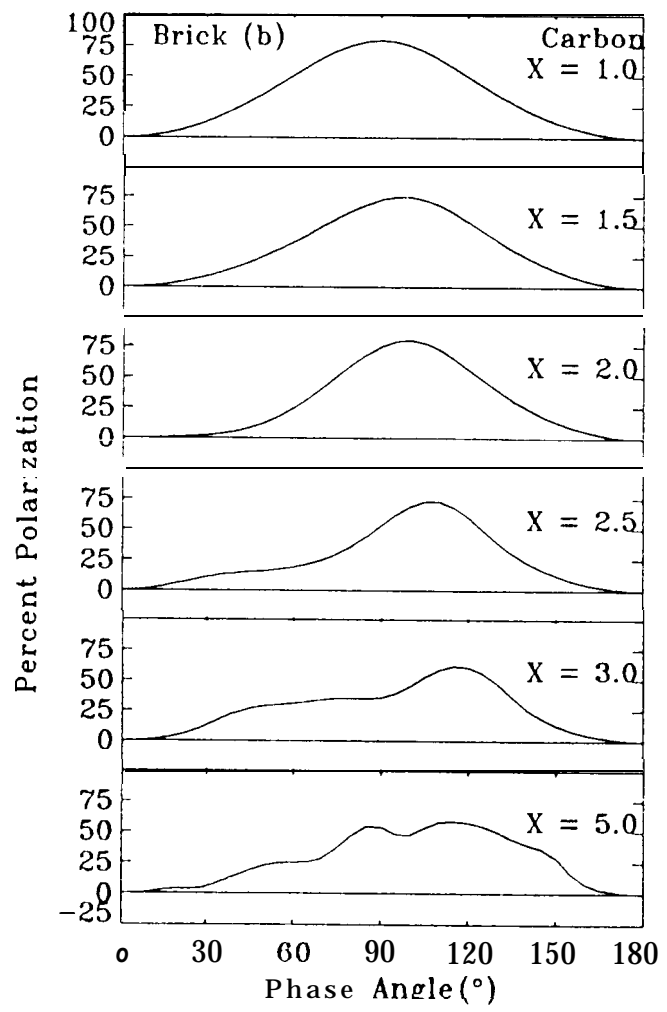
Relative Flux

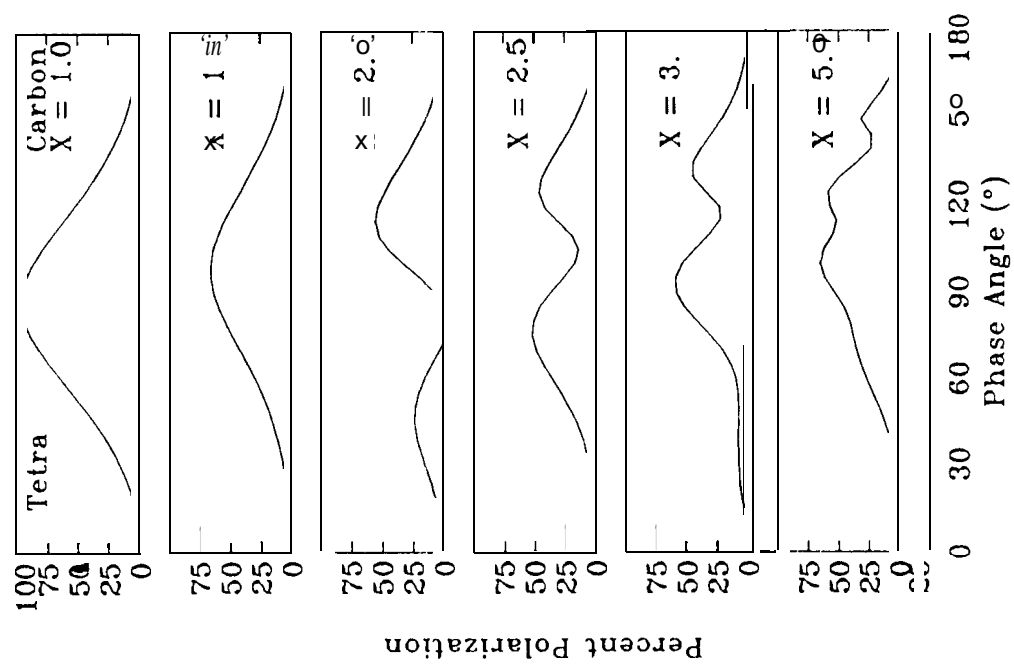


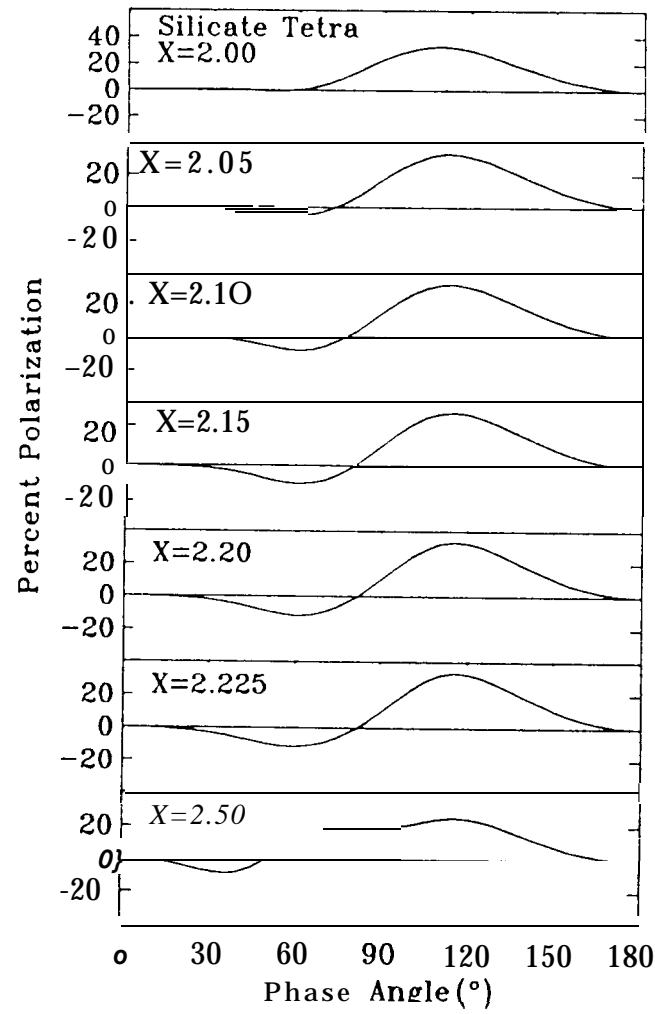


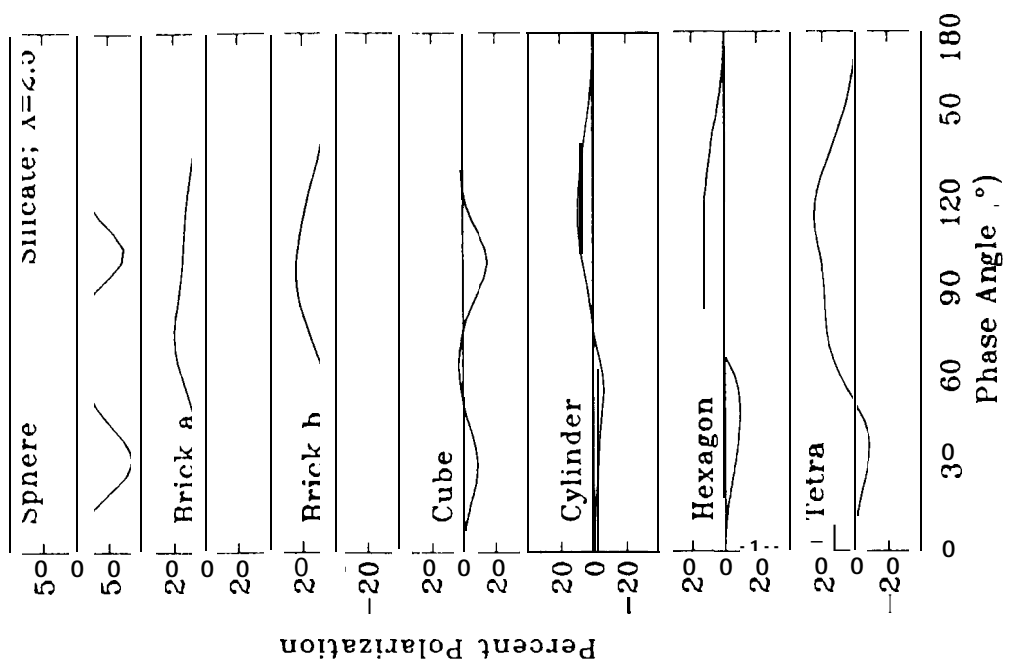


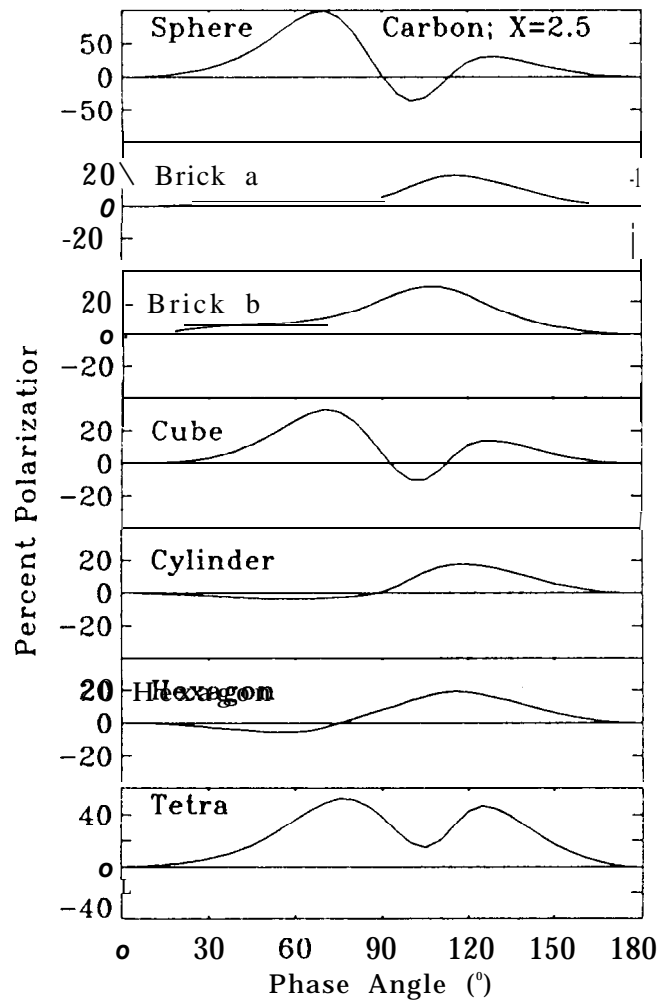


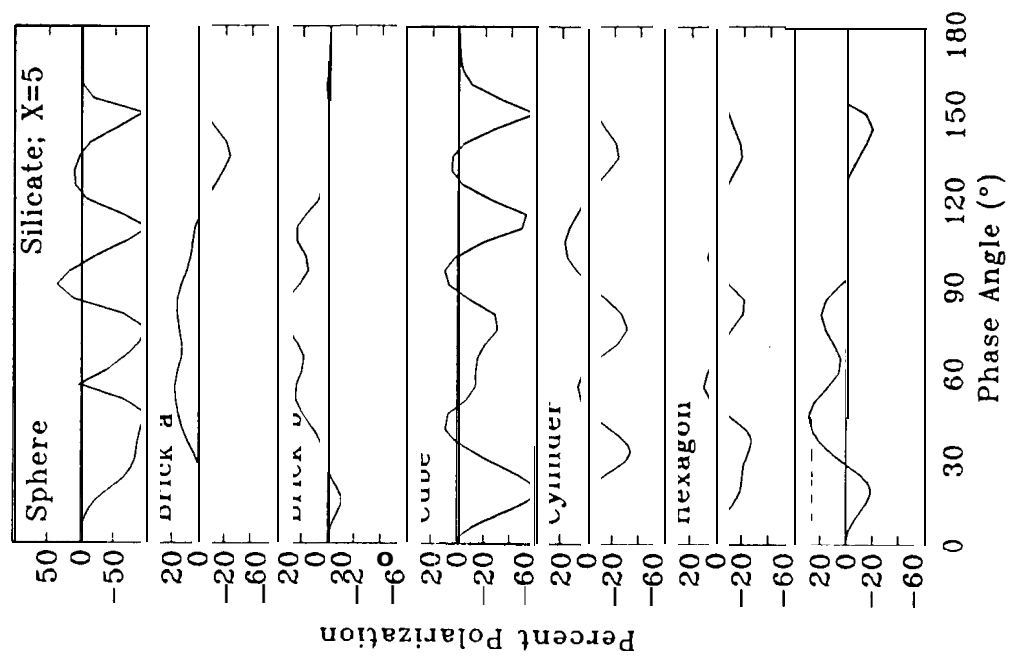


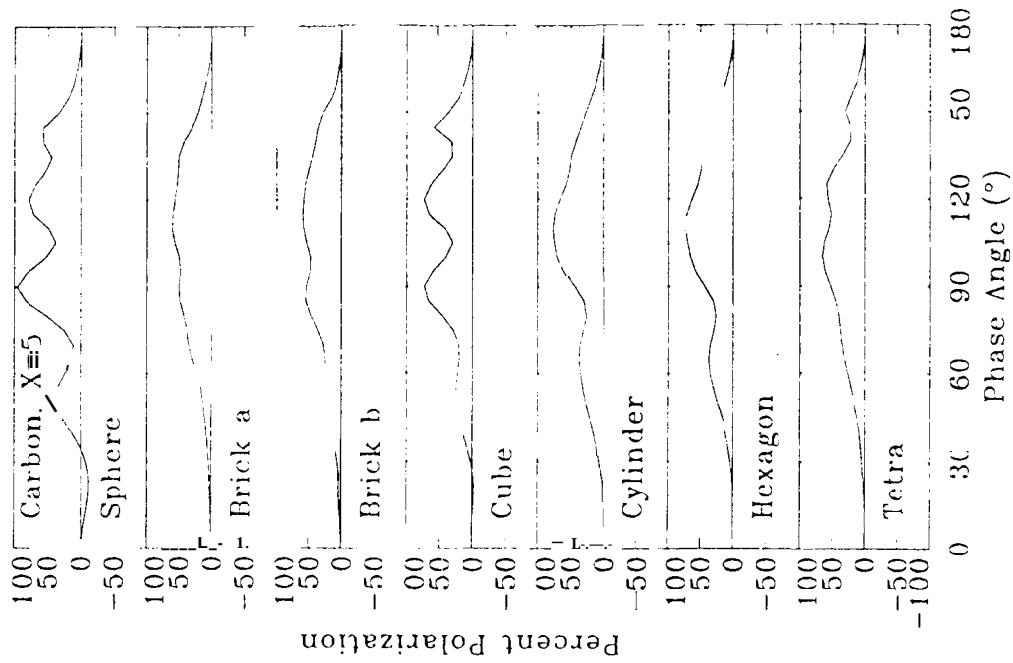


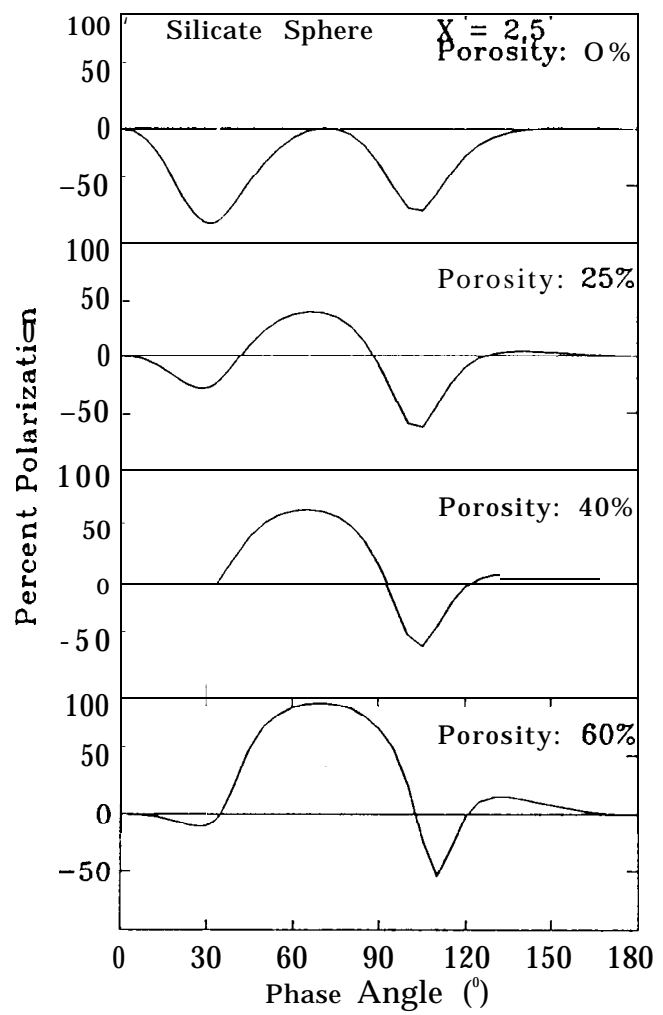


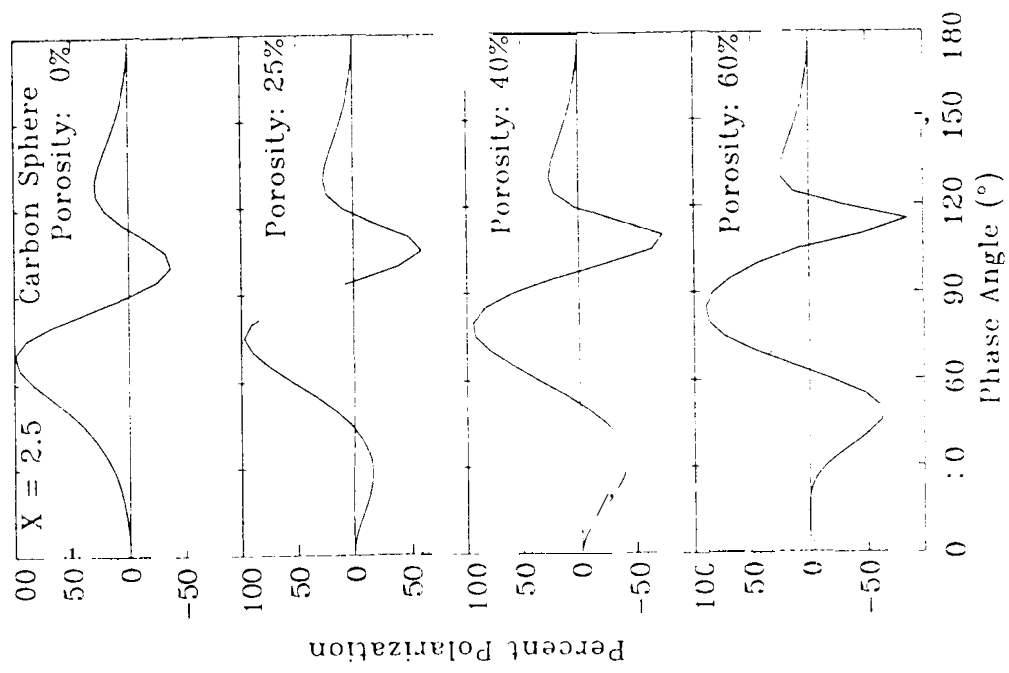


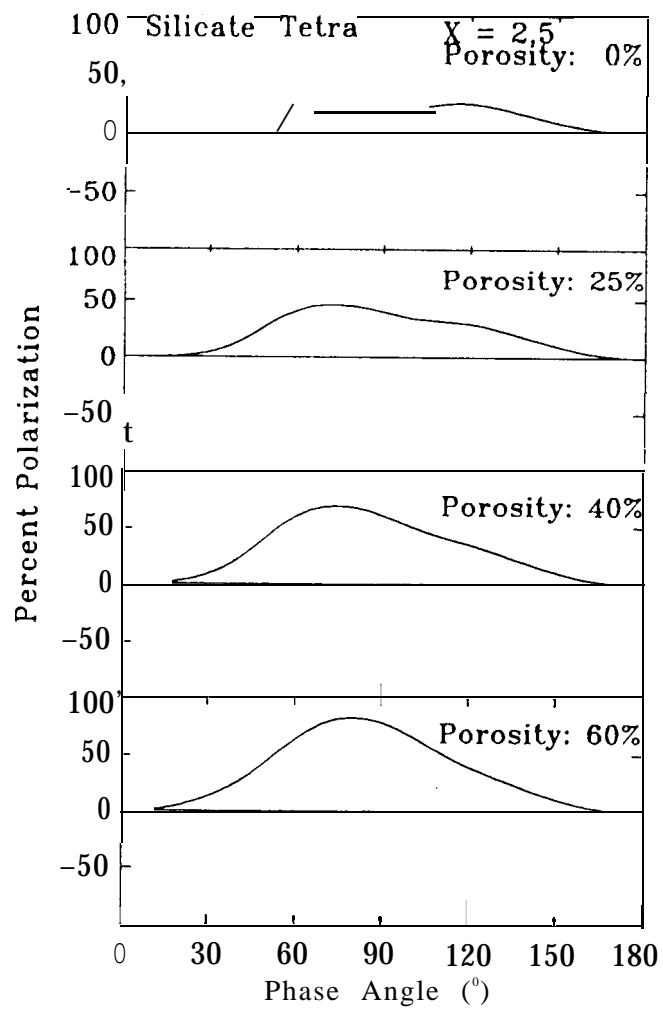


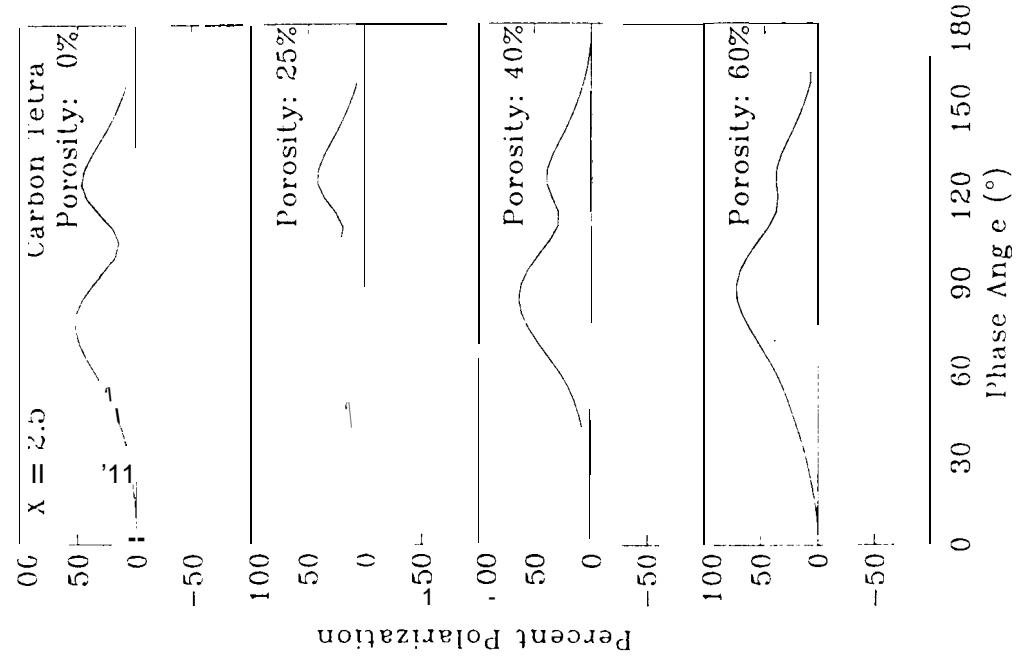


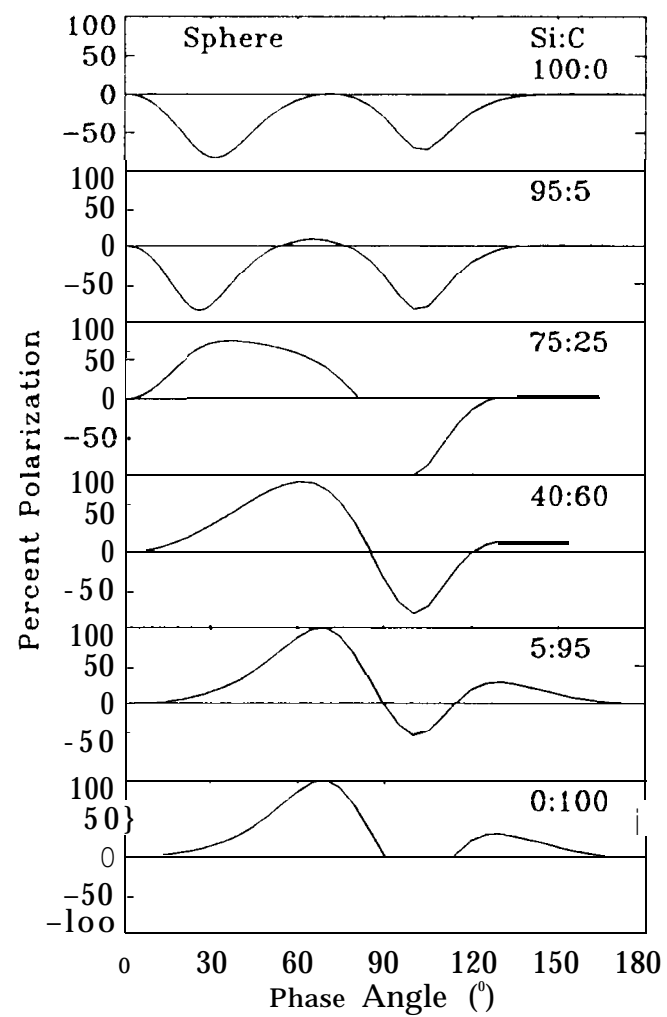


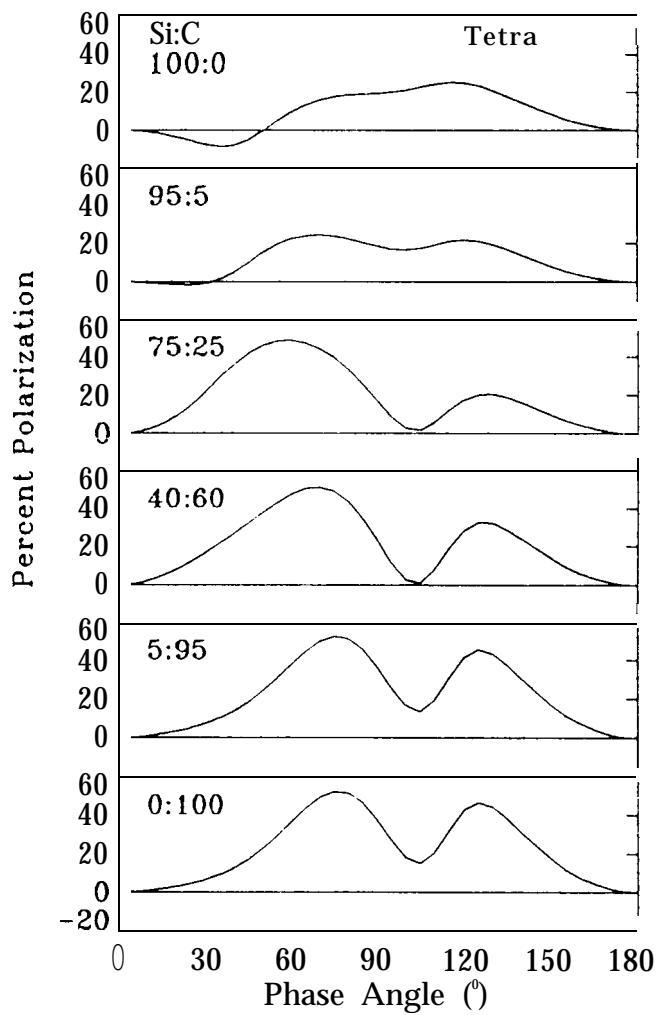


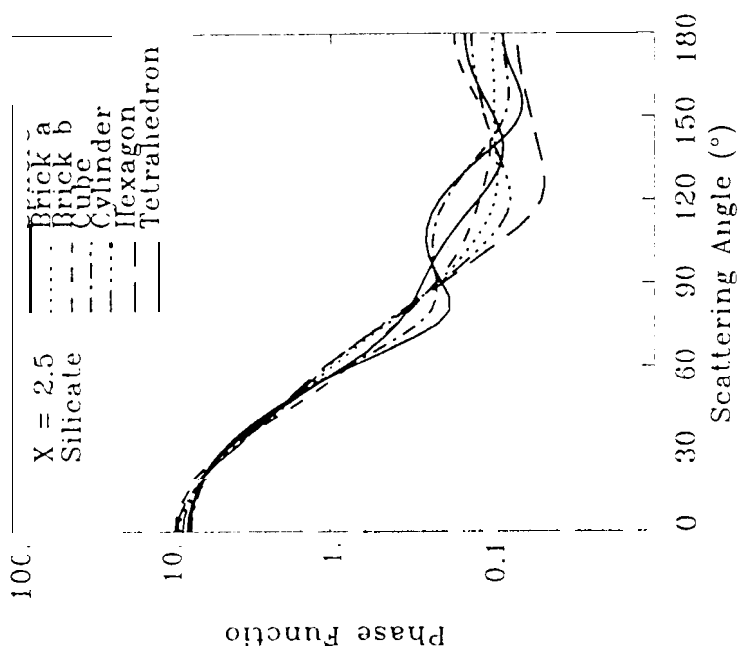
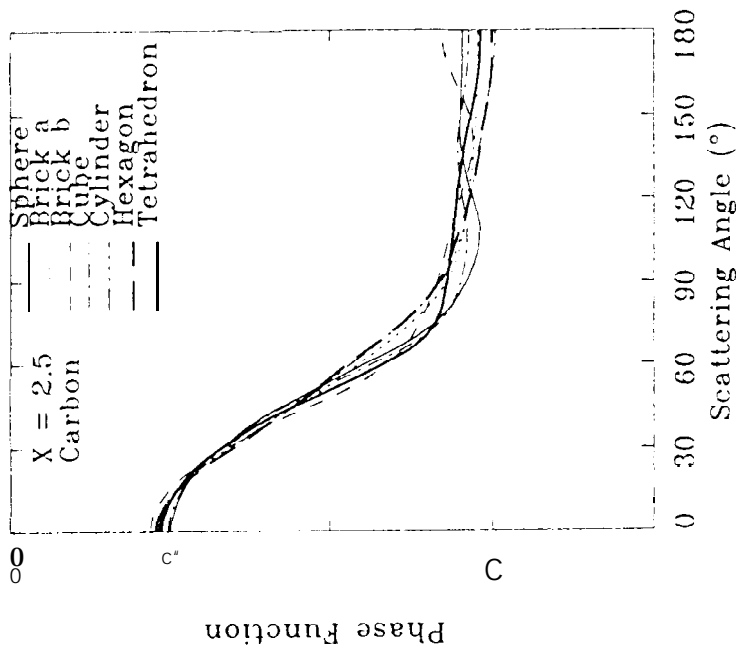


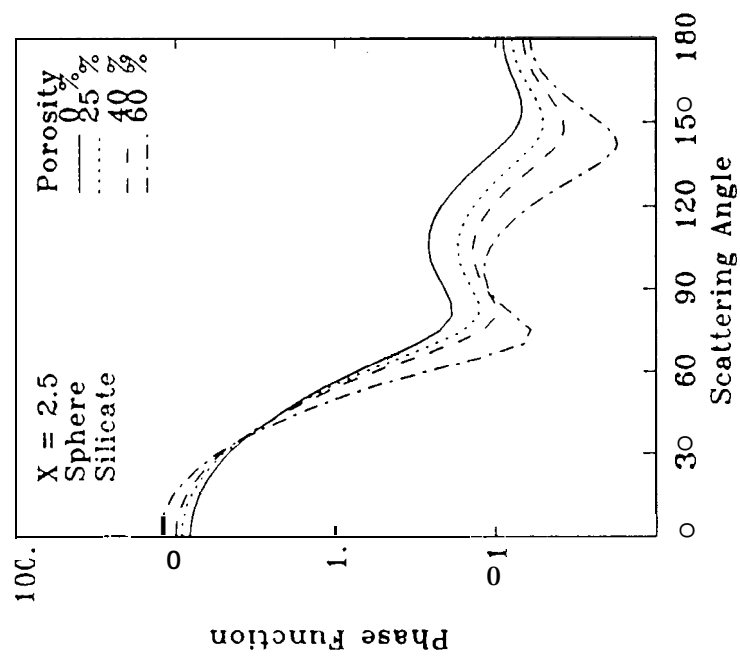
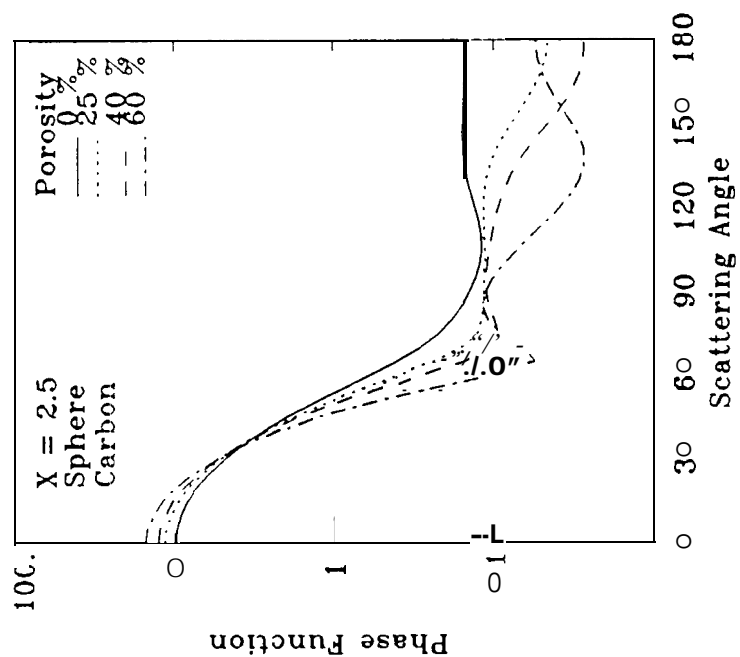


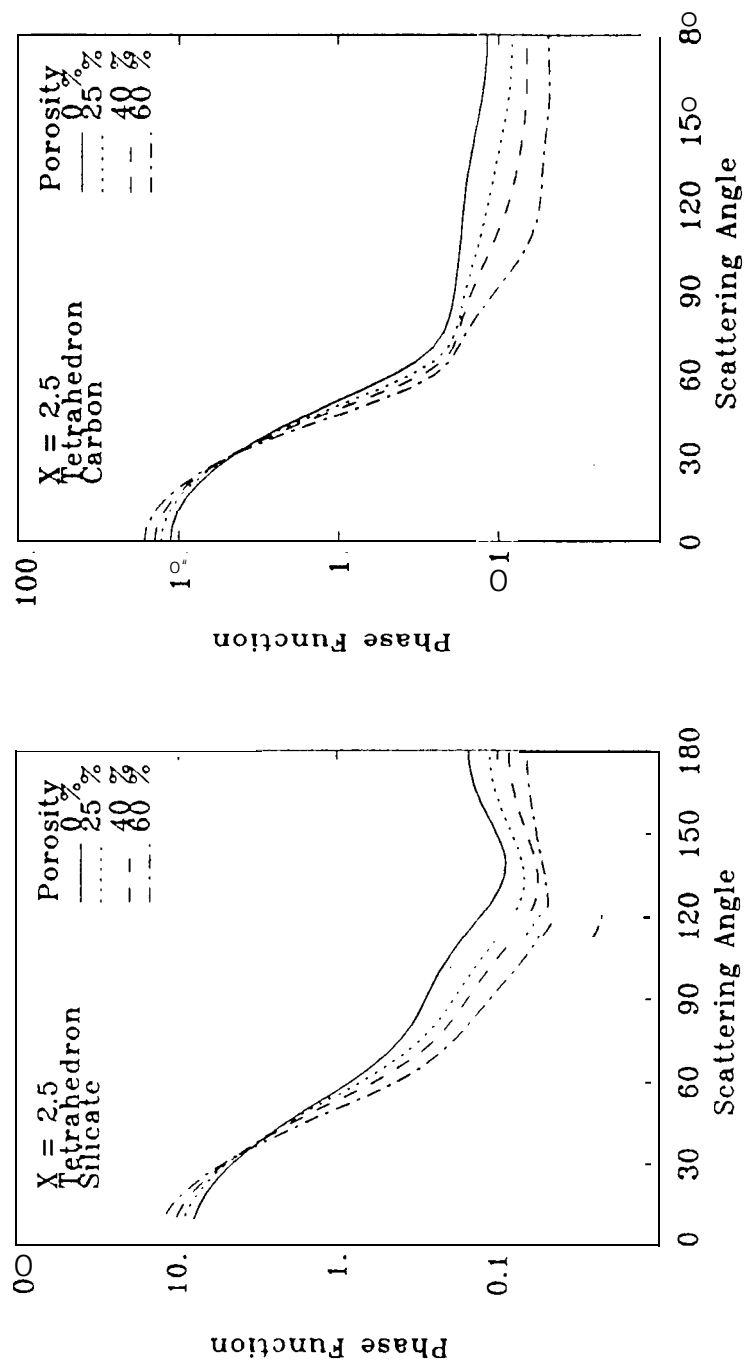


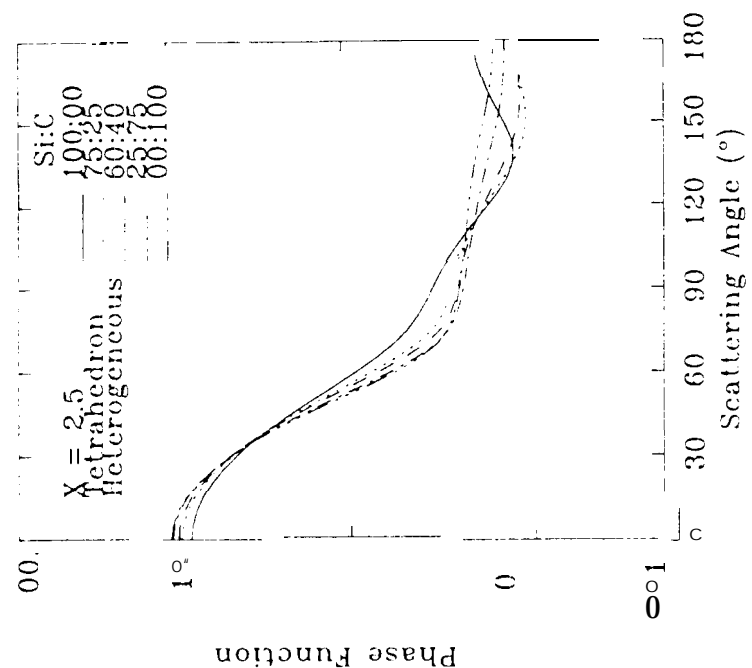


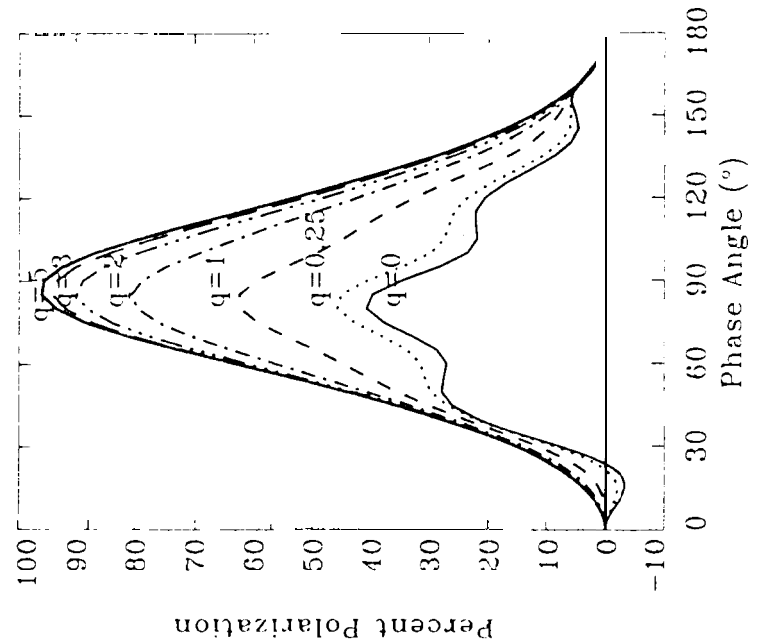
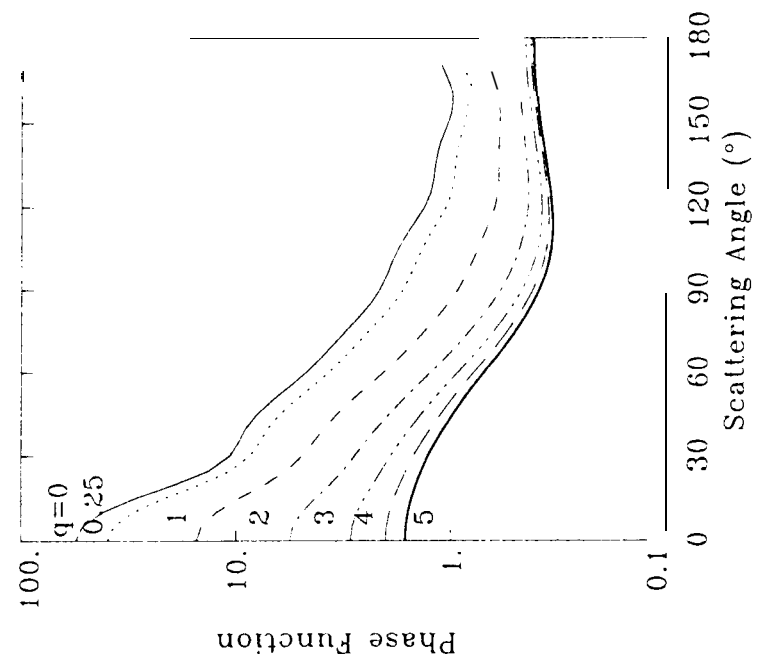


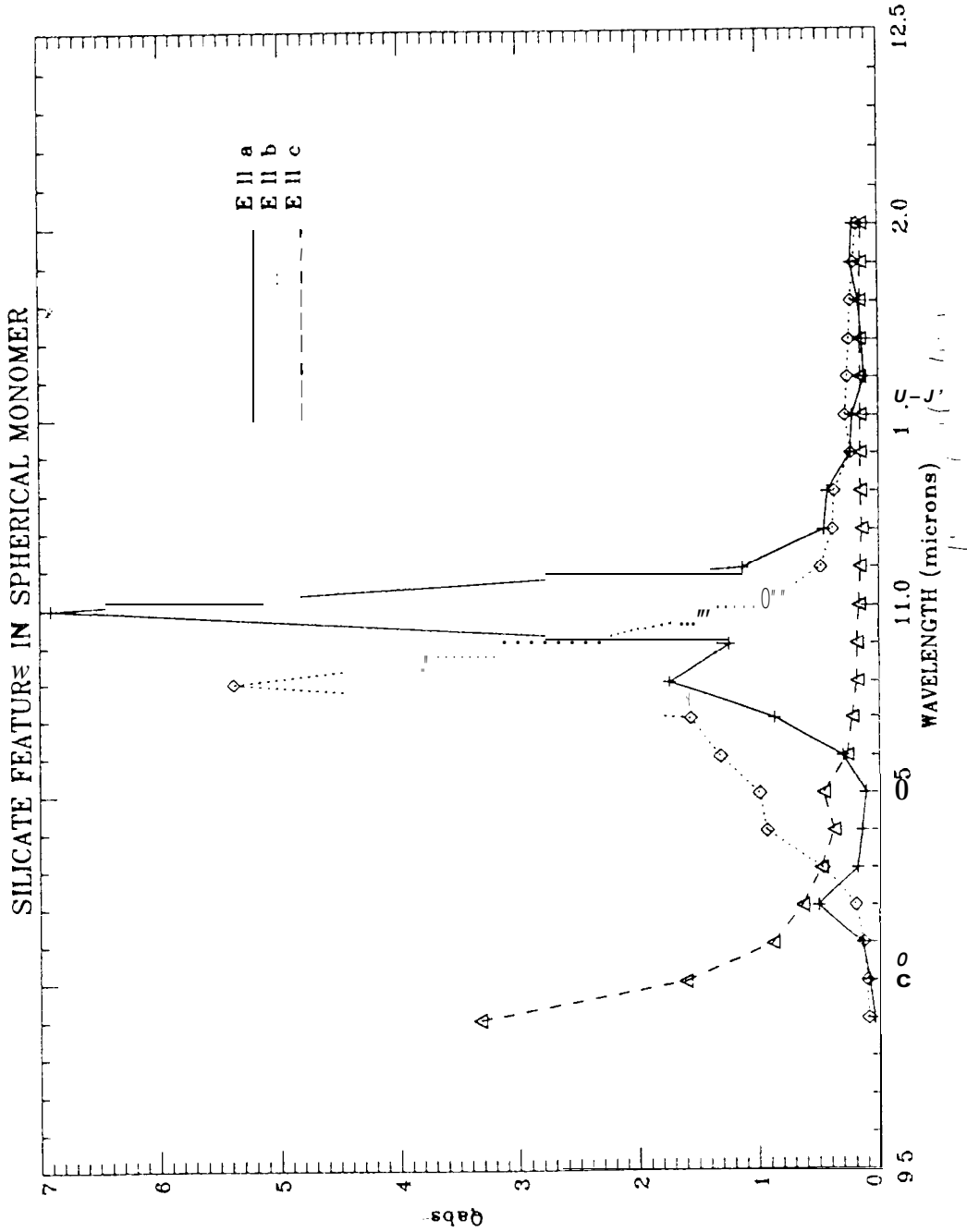


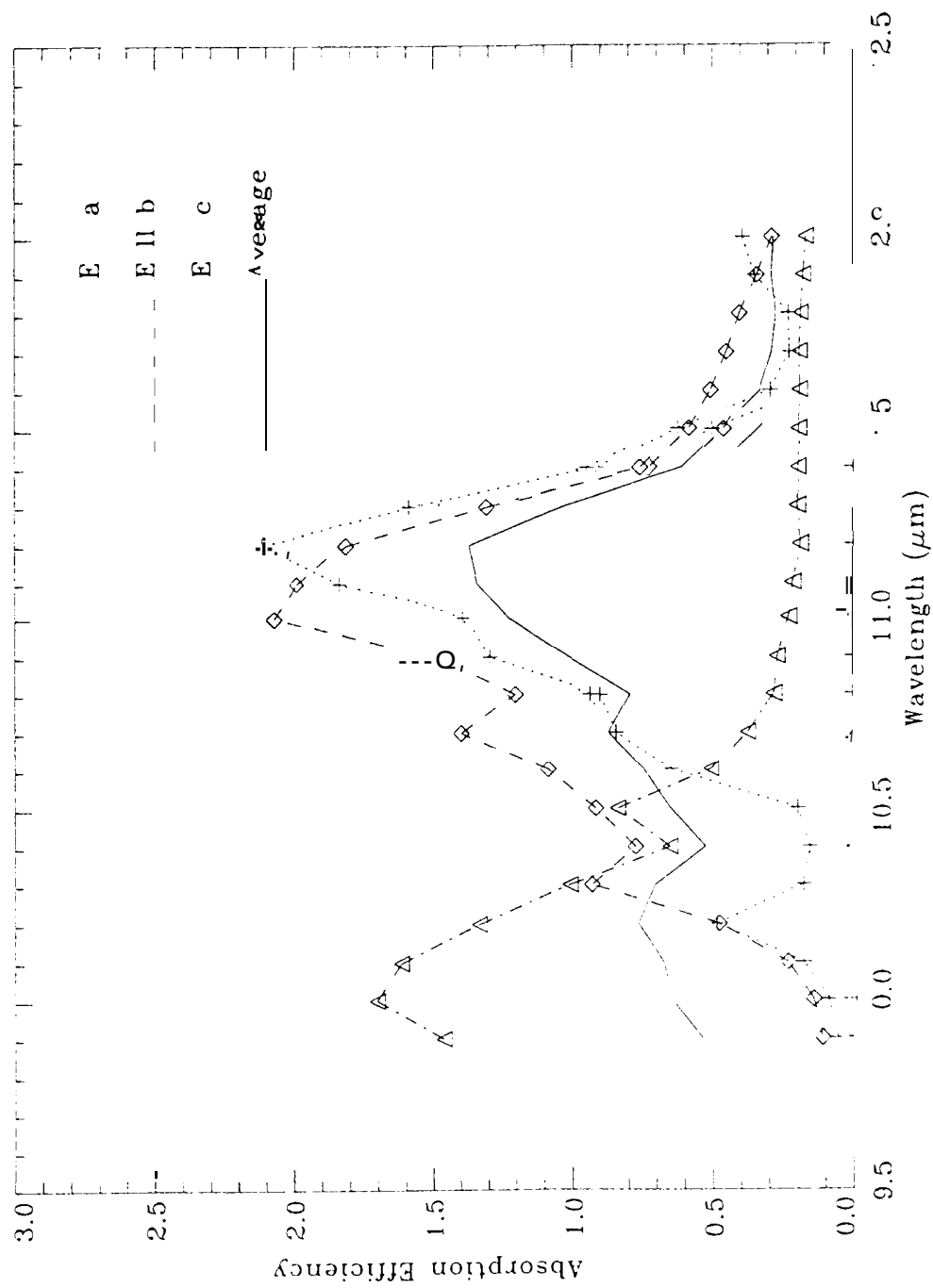


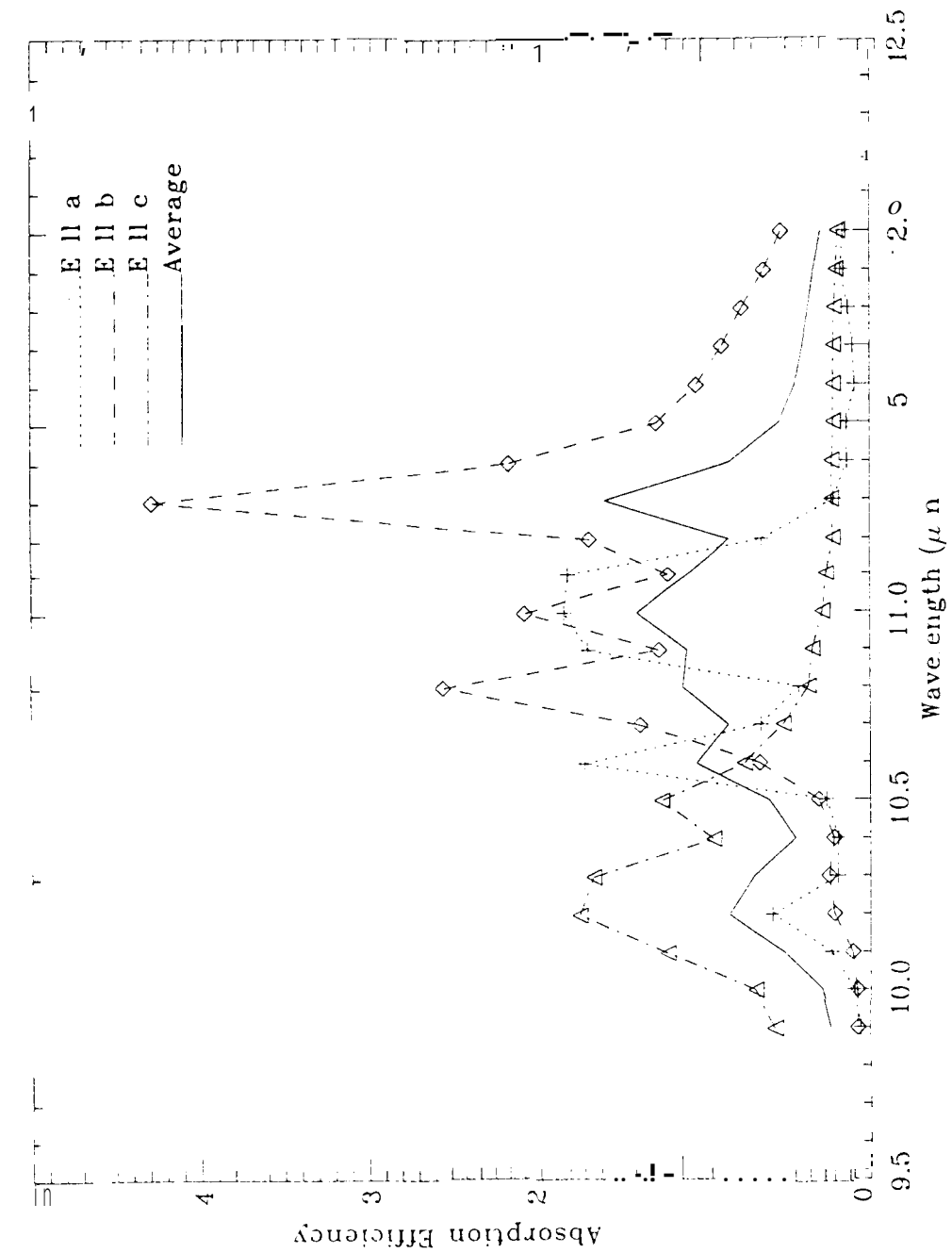




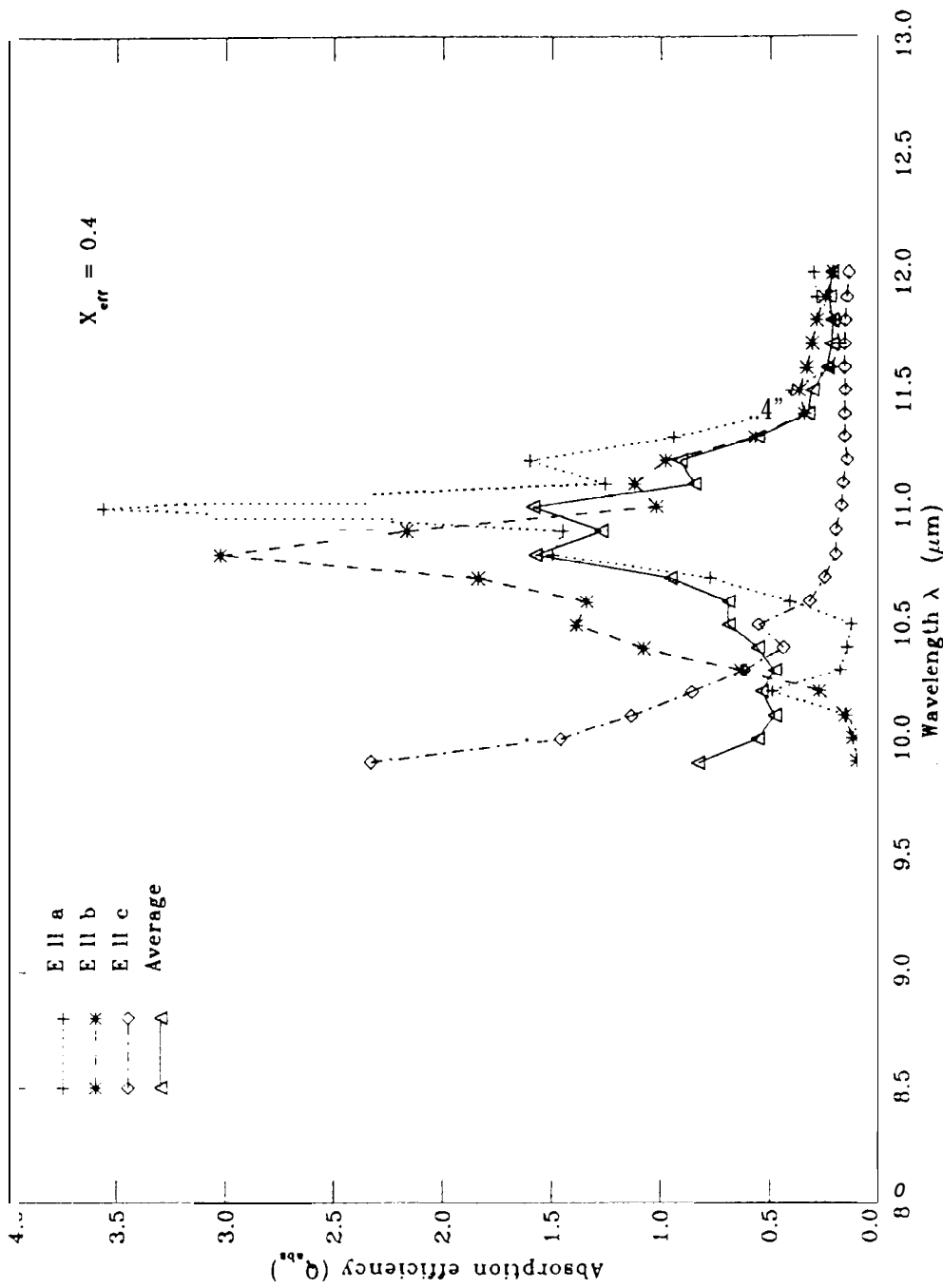








FIVE SPHERICAL MONOMERS



SILICATE FEATURE: TETRAHEDRAL MONOMER AGGREGATES

